J. Fluid Mech. (2023), *vol*. 962, A41, doi:10.1017/jfm.2023.299

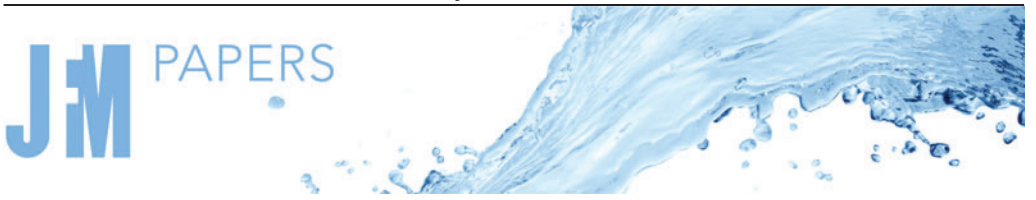

Effect of shear on local boundary layers in turbulent convection

Prafulla P. Shevkar[1], **Sanal K. Mohanan**[1] **and Baburaj A. Puthenveettil**[1],†

[1]Department of Applied Mechanics, Indian Institute of Technology Madras, Chennai 600036, India

(Received 3 May 2022; revised 16 October 2022; accepted 28 March 2023)

In Rayleigh Bénard convection, for a range of Prandtl numbers $4.69 \leqslant Pr \leqslant 5.88$ and Rayleigh numbers $5.52 \times 10^5 \leqslant Ra \leqslant 1.21 \times 10^9$, we study the effect of shear by the inherent large-scale flow (LSF) on the local boundary layers on the hot plate. The velocity distribution in a horizontal plane within the boundary layers at each Ra, at any instant, is (A) unimodal with a peak at approximately the natural convection boundary layer velocities V_{bl}; (B) bimodal with the first peak between V_{bl} and V_L, the shear velocities created by the LSF close to the plate; or (C) unimodal with the peak at approximately V_L. Type A distributions occur more at lower Ra, while type C occur more at higher Ra, with type B occurring more at intermediate Ra. We show that the second peak of the bimodal type B distributions, and the peak of the unimodal type C distributions, scale as V_L scales with Ra. We then show that the areas of such regions that have velocities of the order of V_L increase exponentially with increase in Ra and then saturate. The velocities in the remaining regions, which contribute to the first peak of the bimodal type B distributions and the single peak of type A distributions, are also affected by the shear. We show that the Reynolds number based on these velocities scale as Re_{bs}, the Reynolds number based on the boundary layer velocities forced externally by the shear due to the LSF, which we obtained as a perturbation solution of the scaling relations derived from integral boundary layer equations. For $Pr = 1$ and aspect ratio $\Gamma = 1$, $Re_{bs} \sim Ra^{0.375}$ for small shear, similar to the observed flux scaling in a possible ultimate regime. The velocity at the edge of the natural convection boundary layers was found to increase with Ra as $Ra^{0.35}$; since $V_{bl} \sim Ra^{1/3}$, this suggests a possible shear domination of the boundary layers at high Ra. The effect of shear, however, decreases with increase in Pr and with increase in Γ, and becomes negligible for $Pr \geqslant 100$ at $\Gamma = 1$ or for $\Gamma \geqslant 20$ at $Pr = 1$, causing $Re_{bs} \sim Ra_w^{1/3}$.

Key words: turbulent convection, turbulent boundary layers, Bénard convection

† Email address for correspondence: apbraj@iitm.ac.in

1. Introduction

Turbulent Rayleigh–Bénard convection (RBC) is characterised by diffusive regions near the plates that have boundary layers and thermal plumes, and a turbulent bulk region that has an inherent large-scale flow (LSF) within it. In turn, the LSF, driven by plume columns created by the LSF itself, is expected to act on the boundary layers, thereby modifying their nature. Since the dominant resistance to heat transfer is in the boundary layers, a resulting change in the flux scaling from the classical $1/3$ power law is also expected. However, the exact nature of this modification of the boundary layers due to LSF is not known conclusively. In this study, we bring new insights into how LSF modifies the boundary layers by presenting the evolution of the instantaneous probability density functions (p.d.f.s) of horizontal velocity magnitudes in a horizontal plane close to the hot plate with Rayleigh number. Novel scaling laws, based on the consideration of the modification of the local boundary layers on either sides of the plumes, embedded within a shear boundary layer due to the LSF, are shown to describe the observed variation of the peaks of these p.d.f.s.

It is well known that if heat flux in turbulent RBC has to be independent of the layer height H, then, dimensionally, $Nu \sim Ra^{1/3}$, where $Nu = q/(k\,\Delta T/H)$ is the Nusselt number, and $Ra = g\beta\,\Delta T\,H^3/\nu\alpha$ is the Rayleigh number. Here, q is the heat flux, k is the thermal conductivity, $\Delta T = T_h - T_c$ is the total temperature drop across H, with T_h and T_c the top and bottom wall temperatures, respectively, g is the acceleration due to gravity, β is the coefficient of thermal expansion, ν is the kinematic viscosity, and α is the thermal diffusivity. However, the observed flux scaling is anomalous, showing $Nu \sim Ra^n$ with $n \leqslant 0.31$ for $Ra < 10^{11}$ (Roche *et al.* 2004), n approaching $1/3$ for $10^{10} < Ra < 10^{13}$ (He *et al.* 2012; Iyer *et al.* 2020), and the value of n beyond $Ra = 10^{13}$ being not known conclusively. For $Ra > 10^{13}$, He *et al.* (2012) and Zhu *et al.* (2018) observed $n = 0.38$, which, however, has been suggested to be due to non-Boussinesq effects (Skrbek & Urban 2015; Urban *et al.* 2019) or a low range of Ra (Doering, Toppaladoddi & Wettlaufer 2019), and is contested (Zhu *et al.* 2019). At the same time, for $10^{11} < Ra < 10^{15}$, $n = 1/3$ has been observed by Iyer *et al.* (2020) in low-aspect-ratio ($\Gamma = L/H$) containers, where L is the horizontal dimension of the container.

The value of n being different from $1/3$ implies that the heat flux becomes dependent on H, as expected, due to the modification of the boundary layers by the LSF, whose velocity (V_F) depends on H through the Reynolds number (Re) relation

$$Re = V_F H/\nu = 0.139\, Ra_w^{0.447}\, Pr^{-0.7}, \tag{1.1}$$

at $\Gamma = 1$ (Ahlers, Grossman & Lohse 2009). Here, $Ra_w = Ra/2$ is the near-plate Rayleigh number based on the temperature drop near the plate, $\Delta T_w = T_h - T_B = \Delta T/2$, with T_B being the bulk fluid temperature. Numerous hypotheses about the nature of such modification of the boundary layers have been made, resulting in various boundary layer models in RBC. Among these, the major models are those that assume stable diffusion layers with a mixing zone above them (Castaing *et al.* 1989), a turbulent shear boundary layer (Shraiman & Siggia 1990), a laminar, zero pressure gradient, Prandtl–Blasius boundary layer (PBBL) with no buoyancy effects (Grossmann & Lohse 2000), a Falkner–Skan shear boundary layer with pressure gradient (Shishkina, Horn & Wagner 2013), a laminar mixed convection boundary layer (Ovsyannikov *et al.* 2016), and a turbulent forced convection boundary layer with small buoyancy perturbations (Ching *et al.* 2019). The first three of these models are able to match the flux scaling (Ahlers

et al. 2009; Chilla & Schumacher 2012; Roche 2020), but fail to reproduce the observed profiles of velocity and temperature (Reeuwijk, Jonker & Hanjalić 2008; Sun, Cheung & Xia 2008; Shi, Emran & Schumacher 2012; Wagner, Shishkina & Wagner 2012), as well as the boundary layer thicknesses (Qiu & Xia 1998*a*,*b*; Lam *et al.* 2002; Reeuwijk *et al.* 2008). The remaining models try to obtain the mean velocity and temperature profiles, but the resulting flux scaling does not match the observations (Tai *et al.* 2021); clearly, the nature of boundary layers in RBC, and more importantly, their interaction with LSF, remain unresolved.

All of these models assume a single, steady boundary layer that spans the plate width, and compare the resulting profiles of velocity and temperature with the spatio-temporal mean profiles from experiments and computations; similarly with Nu, where the average Nu is compared. However, in contrast, the dynamics near the hot plate is highly unsteady and spatially inhomogeneous with local boundary layers, possibly natural convection type (Stewartson 1958; Rotem & Classen 1969; Pera & Gebhart 1973*a*), becoming unstable at multiple locations to give rise to line plumes (Pera & Gebhart 1973*b*). These line plumes merge, and move along their length, as well as rise (Puthenveettil, Ananthakrishna & Arakeri 2005; Puthenveettil & Arakeri 2005; Gunasegarane & Puthenveettil 2014), with the LSF also aligning them in shear dominant regions (Rama Reddy & Puthenveettil 2011; Shevkar *et al.* 2019). This results in a complex network of line plumes on the hot surface, which act as channels of heat transport from the plate to the bulk (Shishkina & Wagner 2008), with local boundary layers in between them. Given this high spatial inhomogeneity and temporal unsteadiness, an averaging – which mixes up these local boundary layers and line plumes, along with the LSF – to infer about a global boundary layer, and from which the flux, could be the reason for the lack of success of the available phenomenological models of RBC.

In the absence of external shear, the critical thickness of these local boundary layers on either sides of the line plumes scales as

$$\delta_{nc} = \left(\frac{C_1}{2}\right)^{2/5} Z_w\, Pr^{0.54}, \tag{1.2}$$

where

$$Z_w = \left(\frac{\nu\alpha}{g\beta\,\Delta T_w}\right)^{1/3} = \frac{H}{Ra_w^{1/3}} \tag{1.3}$$

is a length scale near the plate (Theerthan & Arakeri 1998), $Pr = \nu/\alpha$ is the Prandtl number, and $C_1 = 47.5$ (Puthenveettil *et al.* 2011). On the other hand, the PBBL thickness at L, for $\Gamma = 1$, is

$$\delta_{pb} = \frac{0.922H}{\sqrt{Re}} \tag{1.4}$$

(Ahlers *et al.* 2009; Stevens *et al.* 2013). Then $\delta_{nc}/\delta_{pb} \sim Ra_w^{-1/9}$, with $\delta_{nc}/\delta_{pb} \sim 0.1$ at $Ra_w = 10^9$; the local boundary layers are then an order thinner than the shear boundary layer engendered by the LSF, and hence are embedded within them. If a major part of the temperature drop near the plate occurs across these local boundary layers, then (1.2) already implies that $Nu = H/2\delta_{nc} \sim Ra_w^{1/3}$, the classical flux scaling. An immediate possibility then arises that the anomalous flux scaling in RBC is due to the modification of these local boundary layers on either side of the line plumes, embedded within the shear boundary layers, by the shear boundary layer itself.

Such shear-induced modifications of these local boundary layers have been observed as changes in the spacings between these line plumes (Shevkar *et al.* 2019) due to shear-induced changes in the stability (Castaing *et al.* 1989) of the local boundary layers in between. The plume spacings that are log-normally distributed in the absence of shear (Puthenveettil & Arakeri 2005) become more narrowly spread around a single value when plumes align in the presence of shear (Shevkar *et al.* 2019). The mean plume spacing at zero shear,

$$\lambda_0 = C_1\, Pr^{n_1}\, Z_w \tag{1.5}$$

(Theerthan & Arakeri 1998; Puthenveettil & Arakeri 2005; Puthenveettil *et al.* 2011), where $n_1 = 0.1$, is increased to

$$\lambda = \lambda_0 + \frac{Z_{sh} S}{D} \tag{1.6}$$

(Shevkar *et al.* 2019), where $Z_{sh} = \nu/V_L$ is the viscous shear length, with V_L being the shear velocity on the local boundary layers, $S = V_L^3 \alpha/g\beta\,\Delta T_w\,\nu^2 = Re_L^3/Ra_w$ is a shear parameter, with Re_L being the Reynolds number based on V_L and H, and D is a function of Pr. However, it is not known how the shear due to the LSF changes the velocities within these local boundary layers, as well as their thicknesses. These are two crucial pieces of information necessary to understand the shear-induced changes to the nature of these local boundary layers, which could be the key missing piece in understanding the anomalous flux scaling and the near-plate profiles of velocity and temperature, in RBC.

With this aim, the present paper presents the instantaneous spatial velocity fields within these local boundary layers, obtained by stereo particle image velocimetry (PIV) in a horizontal plane, for $10^5 \leqslant Ra \leqslant 10^9$, $4.69 \leqslant Pr \leqslant 5.88$ and $1.71 \leqslant \Gamma \leqslant 10$. We avoid any spatio-temporal averaging of these highly spatially inhomogeneous and temporally unsteady velocity fields, which would mix up the velocities from the local boundary layers, plumes and the LSF. Instead, we study the p.d.f.s of the horizontal velocity magnitudes, which show predominantly a single peak at lower Ra, a double peak at intermediate Ra, and then again a single peak at higher Ra. The peaks of these p.d.f.s keep shifting to higher velocity values with increasing Ra, showing the increasing effect of shear due to the LSF on the velocity field within the local boundary layers. We also observe a corresponding increase in areas affected by shear, first qualitatively, as an increase in areas of regions having aligned velocity vectors of higher magnitudes, and then later quantitatively, as an increase in areas contributing to the second mode in the double-peaked p.d.f.s. The velocities from these shear dominant regions, reflected in the second peak of the double-peaked p.d.f.s and the lone peak from the single mode p.d.f. at higher Ra, scale in the same way as the strength of the LSF scales with Ra. However, interestingly, the first peak from the double-mode p.d.f.s, and the sole peak from the p.d.f.s at lower Ra, scale as $Ra^{0.38}$, possibly in a coincidental way, in the same way as the observed scaling of flux at $Ra > 10^{13}$. We then show that this scaling can occur when a natural convection boundary layer, embedded within a shear boundary layer due to the LSF, is forced externally by the same shear boundary layer. In such a scenario, with increasing shear, we show that these local boundary layers can become mixed convection boundary layers, and then later at large shear, PBBLs. Our model predicts that the shear at the edge of these local boundary layers increases with Ra, more than the increase of buoyant velocities within the boundary layers with Ra, thereby making these boundary layers more shear-dominant with increase in Ra. This prediction, however, needs to be qualified since changes in plume

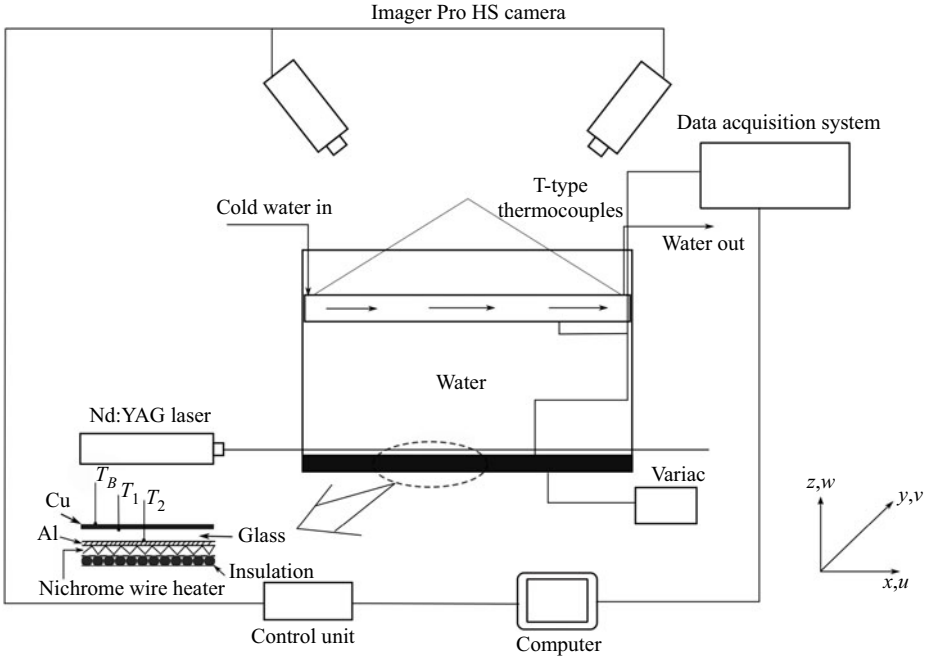

Figure 1. Schematic of the experimental set-up.

spacing and local boundary layer thicknesses, which could be significant at larger Ra, were neglected.

The paper is organised as follows. We first describe our PIV experiments in water at various Γ in § 2. The horizontal velocity fields within the local boundary layers, the characteristics of the p.d.f.s of horizontal velocity magnitudes, the evolution of the shear-affected areas, and that of the number of different types of p.d.f.s with Ra, as well as the experimental scaling of the peaks of the p.d.f.s, are described in § 3. Section 4 details the theoretical scaling analysis where the scaling equations (§ 4.1), obtained from the integral natural convection boundary layer equations forced by an external shear (Appendix A), are solved by perturbations methods (§ 4.2) to obtain the velocity boundary layer thickness (§ 4.3) and the dimensionless shear (§ 4.4) at the edge of the local boundary layers. These are then used to obtain the scaling of the characteristic Reynolds number within the local boundary layers, forced externally by the shear due to the LSF. The obtained scaling is shown to match the observations in § 4.5, before we conclude in § 5.

2. RBC experiments in water

Statistically steady, turbulent, RBC experiments were conducted in a glass tank, having cross-sectional area 30 cm × 30 cm and insulated from the sides, within which a water column of height H was confined between a hot copper plate at the bottom and a cool glass chamber at the top, through which water at constant temperature was circulated. The bottom Cu plate was maintained at a constant heat flux by a nichrome wire heater embedded within a plate assembly, as shown in figure 1, and connected to a variac. The heat flux into the Cu plate (q) and H were varied to obtain the range of values of Ra and Pr given in table 1. The heat flux was estimated from the average temperature drop across the glass plate in the plate assembly, which was calculated from T-type thermocouples located

https://doi.org/10.1017/jfm.2023.299 Published online by Cambridge University Press

Ra	Pr	ΔT (°C)	T_B (°C)	H (cm)	Γ	h_m (mm)	h_F (mm)	A_i (mm^2)	δ_{pb} (mm)	δ_{nc} (mm)	V_{bl} (mm s^{-1})	V_L (mm s^{-1})	V_F (mm s^{-1})	w_{pl} (mm s^{-1})	Δt (s)	ν (m s^{-2}) ($\times 10^{-8}$)
5.52×10^5	5.88	0.99	26.52	3	10	2.7	—	75×64	8.39	4.26	0.62	1.27	0.99	1.45	0.1	86.33
3.32×10^6	5.21	4.86	31.63	3	10	1.5	7.5	73 × 61	5.38	2.19	1.14	2.75	2.14	2.59	0.1	77.40
2.37×10^7	5.69	3.17	27.97	7	4.29	1.8	—	76 × 65	8.36	2.79	0.93	2.87	3.61	2.15	0.0667	83.60
2.62×10^7	5.59	3.44	28.66	7	4.29	1.6	—	76 × 66	8.12	2.67	0.97	2.99	3.76	2.18	0.1	82.30
3.99×10^7	5.27	4.81	31.10	7	4.29	1.5	17.5	75 × 63	7.24	2.25	1.12	3.56	4.49	2.53	0.1	78.22
2.19×10^8	5.24	5.17	31.42	12	2.5	1.5	4	75 × 64	8.46	2.18	1.15	4.42	7.58	2.62	0.0667	77.84
4.41×10^8	5.30	5.33	30.90	15	2.0	1.0	—	75 × 63	9.08	2.17	1.16	4.84	9.43	2.45	0.0667	78.63
5.59×10^8	5.18	6.54	31.88	15	2.0	1.0	—	74 × 63	8.55	1.98	1.26	5.35	10.42	2.68	0.0667	77.05
6.30×10^8	5.00	7.12	33.38	15	2.0	1.0	4	107 × 87	8.22	1.87	1.32	5.61	10.92	2.80	0.0667	74.73
8.08×10^8	4.69	8.24	36.30	15	2.0	1.0	4, 10	75 × 63	7.59	1.66	1.44	6.18	12.03	3.07	0.0667	70.60
1.21×10^9	5.09	9.16	32.60	17.54	1.71	1.3	4	76 × 66	8.35	1.77	1.40	6.43	13.66	3.19	0.0667	75.94

Table 1. Values of the experimental parameters and the parameters for the PIV measurements used in the present study. All the fluid properties were estimated at T_B, the bulk fluid temperature. The size of the square interrogation window (D_I) was 32 pixels, and the overlap was 50 % at all Ra.

Ra_w	2.76×10^5	1.66×10^6	1.31×10^7	1.10×10^8	6.05×10^8
Number of p.d.f.s	4197	1399	11 192	11 192	11 192

Table 2. Total number of p.d.f.s at each Ra_w.

at three different horizontal positions across the glass plate. The temperatures of the hot Cu plate at the bottom and the cold glass plate at the top were measured at two different horizontal locations at the surface of the plates by T-type thermocouples. The average bottom and top plate temperatures, T_h and T_c, calculated from these measurements, were used to calculate the constant temperature difference $\Delta T = T_h - T_c$ across the fluid layer, given in table 1. The error in temperature measurement was 0.02 °C, as estimated from repeated measurements of known temperatures.

The velocity field in a horizontal (x–y) plane close to the bottom hot plate was obtained by stereo PIV in a single-pulse, single-frame mode at all Ra. Since the height of the measurement plane (h_m) was set so that $Z_w/h_m \approx 0.2$, h_m was within the natural convection velocity boundary layer thickness δ_{nc} (see (1.2)), and within the PBBL thickness δ_{pb} (see (1.4)). The flow was seeded with neutrally buoyant polyamide particles (density $\rho_p = 1.012$ g cm^{-3}) of mean diameter 55 μm, which were illuminated by a laser sheet of thickness $l_t = 1$ mm from an Nd:YAG laser (Litron, 100 mJ pulse^{-1}). The particles followed the flow since the Stokes number was less than 4.2×10^{-3}. Two Imager Pro HS (LaVision GmbH) double-shutter cameras (1024 × 1280 pixels), oriented at 32.5° with the vertical from above, were used to capture particle images of area $A_i = L_i \times W_i$ at the centre of the plate in a single-frame mode; the values of A_i for each Ra are given in table 1. Refraction errors were minimised by viewing the bottom plate through a water-filled prism placed over the top of the cold chamber, and by using a third-order polynomial mapping function obtained by imaging a calibration plate. The times between the laser pulses (Δt), given in table 1, were chosen such that the highest out-of-plane particle displacements, due to the plume centre line vertical velocities, in the plane of measurement,

$$w_{pl} = 1.5\, Pr^{0.27}\, \frac{\alpha}{h_m}\, Ra_{h_m}^{2/5} \tag{2.1}$$

(Gunasegarane & Puthenveettil 2014), where Ra_{h_m} is the Rayleigh number based on ΔT and h_m, were not more than $l_t/4$. The maximum in-plane particle displacements corresponding to these Δt were approximately 10 pixels at each Ra. The frame rates of the single frames from each camera were varied from $1/t_f = 10$ Hz at the lowest Ra to 15 Hz at the highest Ra, synchronous with the pulses from the laser.

A multipass adaptive window stereo cross-correlation method (DaVis, LaVision GMBH) was used on the successive frames from each camera to calculate the two-dimensional, three-component spatial vector fields in a horizontal plane at height h_m from the bottom plate with frequency $1/t_f$, for a time period of at least ten LSF circulation times. The size of the square interrogation window ($D_I = 32$ pixels) and the particle concentrations were chosen so that the displacement of particles was $x_p \leqslant D_I/4$, and at least 10 particles were present in an interrogation window at any time. Spurious vectors, removed by applying a median filter of 3 pix × 3 pix neighbourhood, were replaced by interpolated vectors. A Gaussian low-pass filter with kernel defined over a 9 × 9 matrix was applied on the final vector field to reduce the noise. The spatial resolution L_v for all

the vector fields at each Ra was approximately 1 mm, except at $Ra = 6.3 \times 10^8$, where it was 1.4 mm; the parameters for PIV, used for each Ra, are listed in table 1.

3. Probability density functions of horizontal velocities

3.1. *Procedure to obtain the p.d.f.s*

To understand the velocities of dominant motions within the boundary layers, we now study the instantaneous p.d.f.s of $U = \sqrt{u^2 + v^2}$, the magnitude of the horizontal velocities within the local boundary layers, where u and v are the fluid velocities in the x and y directions, respectively. These instantaneous p.d.f.s were estimated from the instantaneous PIV velocity fields in horizontal planes at heights $h_m < \delta_{nc} \ll \delta_{pb}$, given in table 1, at each Ra_w. An in-house code generated the instantaneous p.d.f.s using the following iterative procedure on each instantaneous spatial velocity field, separated temporally by t_f, from a set having 1399 such velocity fields; 1–8 such sets, separated temporally by 210 s, were used at each Ra_w to span at least 10 LSF times.

At any instant, an initial p.d.f. was first obtained from the spatial velocity field using 50 bins of equal sizes as

$$\text{p.d.f.} = \frac{N_U}{sb}, \tag{3.1}$$

where N_U is the number of occurrences of U in each bin, s is the sample size of U, and b is the bin size. We then proceed to estimate the total number of dominant peaks occurring in the p.d.f.s, so as to classify these p.d.f.s in the following way. In this calculation, since we are interested in the velocities of the dominant motions, peaks with N_U less than 10 % of the N_U of the highest peak are neglected. The minimum allowed separation between the peaks was kept equal to $\frac{1}{4}(V_L/V_{bl} - 1)$, to minimise the possibility of counting peaks due to fluctuations as dominant peaks. Here, V_L is the shear on the local boundary layers, estimated as the velocity of longitudinal motion of plumes by Gunasegarane & Puthenveettil (2014), given through the corresponding Reynolds number

$$Re_L = V_L H/\nu = 0.55\, Ra_w^{4/9}\, Pr^{-2/3}. \tag{3.2}$$

Here, V_{bl} is the characteristic velocity in the local natural convection boundary layer (NCBL), given through the corresponding Reynolds number

$$Re_{bl} = V_{bl} H/\nu = 1.88\, Ra_w^{1/3}\, Pr^{-0.98} \tag{3.3}$$

(Vipin 2013; Gunasegarane & Puthenveettil 2014). The rarely occurring fluctuations at the tails of the p.d.f.s, similar to that at $U/V_{bl} \approx 7.75$ in figure 2(*e*), are also neglected in this estimation.

If the number of maxima detected by this procedure was greater than two, then the p.d.f. was recalculated by reducing the number of bins by one in successive iterations until the number of maxima became less than or equal to two. The iteration was stopped when the number of bins became 10, before two or fewer dominant peaks were detected. In such a case, peaks with frequencies less than 11 % of the frequency of the highest peak in the p.d.f. were neglected, and the above iterative process, with the initial number of bins equal to 50, was repeated. After this process, in the rare instances where the number of bins was still $\leqslant 10$ with the number of peaks being >2, the cut-off frequency was further increased to 12 % and the process repeated until a smooth p.d.f. with number of bins $\geqslant 10$ and number of peaks $\leqslant 2$ was obtained.

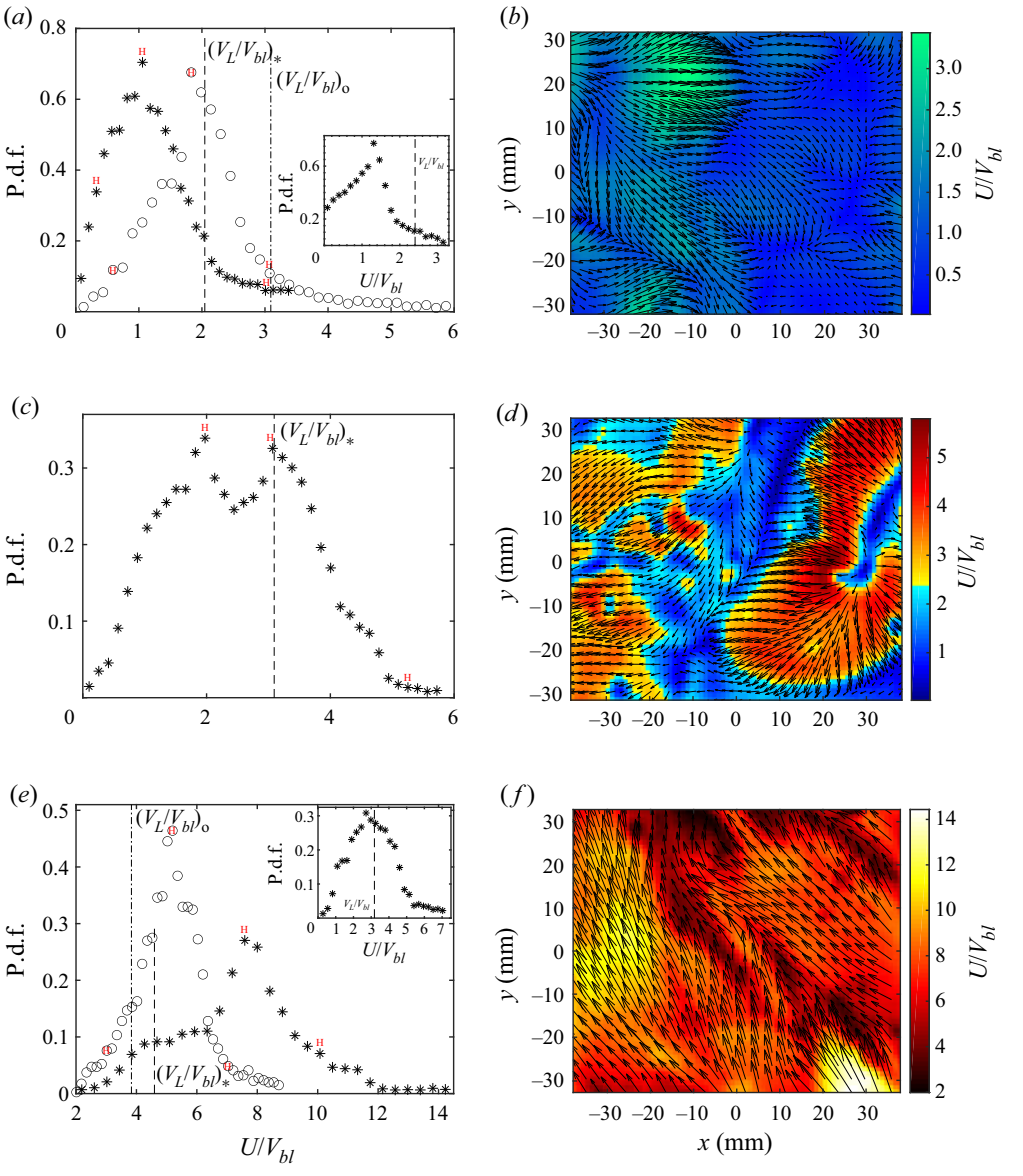

Figure 2. Instantaneous p.d.f.s of the dimensionless horizontal velocity magnitudes and the corresponding instantaneous spatial distributions of horizontal velocity vectors overlaid over the dimensionless horizontal velocity magnitudes at three Ra_w. Values of (Ra_w, Γ, Re_F) for $*$ are: (*a*,*b*) $(2.76 \times 10^5, 10, 34.42)$; (*c*,*d*) $(1.31 \times 10^7, 4.3, 320)$; (*e*,*f*) $(6.05 \times 10^8, 1.71, 3148)$. Values for $\circ$ are: (*a*) $(1.31 \times 10^7, 4.3, 320)$; (*e*) $(1.10 \times 10^8, 2.5, 1169)$. In insets, values for $*$ are: (*a*) $(1.66 \times 10^6, 10, 82.86)$; (*e*) $(2 \times 10^7, 4.3, 401.6)$. The values of V_L/V_{bl} corresponding to $*$ and $\circ$ are shown by dashed lines and dash-dotted lines, respectively, in (*a*,*c*,*e*). The error bars in (*a*,*c*,*e*) show the maximum uncertainties 7.1 %, 2.5 % and 4 % at $U/V_{bl} = 0.6$, 2 and 3, respectively. Details of error analysis can be found in Appendix C.

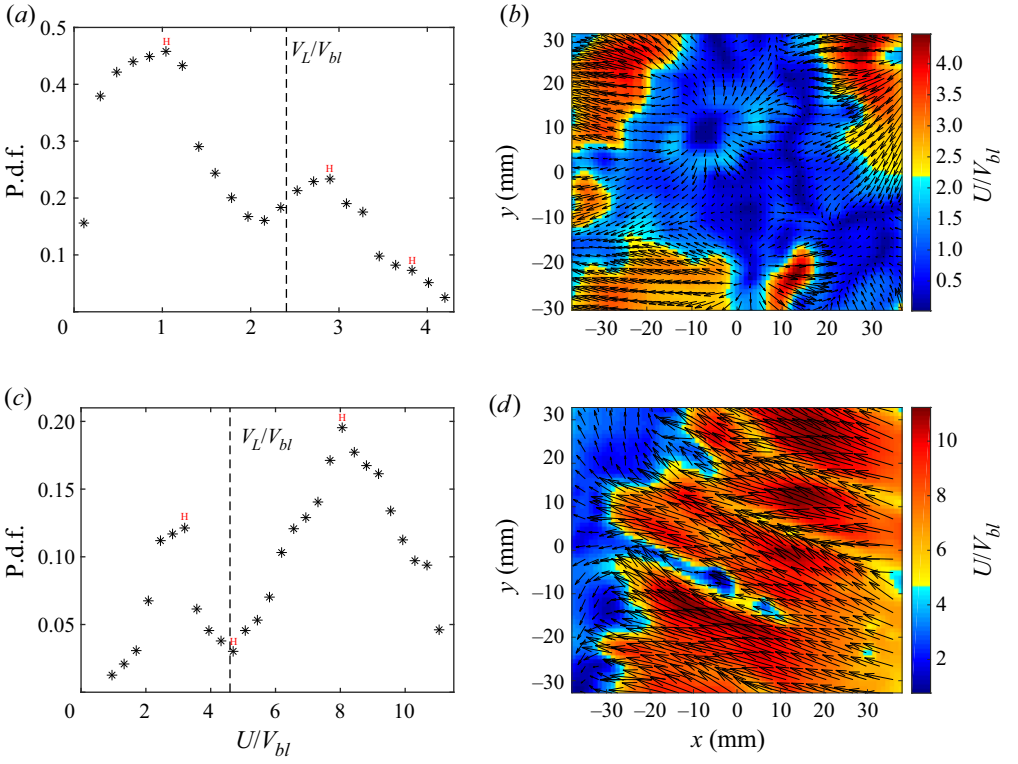

Figure 3. Instantaneous bimodal p.d.f.s of dimensionless horizontal velocity magnitudes, and the corresponding instantaneous spatial distributions of dimensionless horizontal velocity vectors, overlaid over the dimensionless horizontal velocity magnitudes, at intermediate and high Ra_w: (*a*,*b*) $(Ra_w, \Gamma, Re_F) = (1.66 \times 10^6, 10, 82.86)$; (*c*,*d*) $(Ra_w, \Gamma, Re_F) = (6.05 \times 10^8, 1.71, 3148)$. The error bars in (*a*,*c*) show the maximum uncertainties of 3.8% and 4.9 % at $U/V_{bl} = 1.04$ and 3.2, respectively. Details of error analysis can be found in Appendix C.

3.2. *Types of p.d.f.s*

In the present study, Ra_w was increased from the lowest value $Ra_w = 2.76 \times 10^5$ to the highest value $Ra_w = 6.05 \times 10^8$ by changing the temperature difference ΔT and the cell height H. To increase Ra_w, (i) the cell height was kept constant and ΔT was increased, or (ii) both ΔT and H were increased. Then, with increasing Ra_w, the aspect ratio $\Gamma = L/H$ in the experiments could either be a constant for the first case, or decrease monotonically for the second case. As shown in table 1, the aspect ratio changed from 10 at $Ra_w = 2.76 \times 10^5$ to 1.71 at $Ra_w = 6.05 \times 10^8$. However, in both of these cases, since the Reynolds number based on the LSF velocity V_F scaled as $Re_F \sim Ra_w^{4/9} \Gamma^{-0.57}$ (see (B1)), V_F increased monotonically with increase in Ra_w, whether this increase in Re_F occurred due to the increase in ΔT at a fixed Γ or due to a decreasing Γ, shown in table 1. This increasing V_F with increasing Ra_w changed the shapes of the p.d.f.s and the locations of their peaks. So the change in the p.d.f. shapes and their peaks in the present study, shown in figures 2, 3 and 4, was occurring primarily due to increase in Re_F, whether this increase in Re_F occurred due to increasing Ra_w and/or due to decreasing Γ.

Three different types of instantaneous p.d.f.s, obtained using the above procedure, at $Ra_w = 2.76 \times 10^5, 1.31 \times 10^7, 6.05 \times 10^8$, are shown in figures 2(*a*), 2(*c*) and 2(*e*),

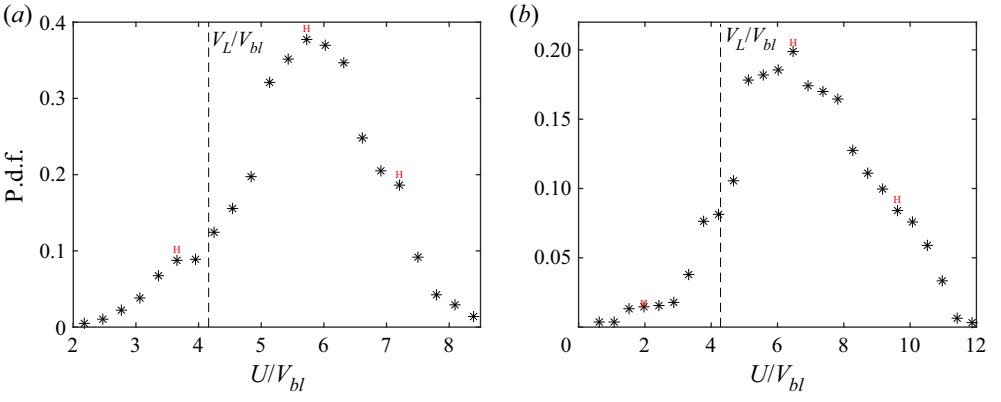

Figure 4. Instantaneous, type C p.d.f.s of dimensionless horizontal velocity magnitudes for two different Ra_w at fixed Γ: (*a*) $(Ra_w, \Gamma, Re_F) = (2.21 \times 10^8, 2, 1800)$; (*b*) $(Ra_w, \Gamma, Re_F) = (4.04 \times 10^8, 2, 2557)$. The error bars show the maximum uncertainties 2.1 % and 7 % at $U/V_{bl} = 3.66$ and 1.97, respectively. Details of error analysis can be found in Appendix C.

respectively. The corresponding horizontal velocity fields in a horizontal plane at height h_m are shown in figures 2(*b*), 2(*d*) and 2(*f*), respectively. P.d.f.s in figures 2(*a*) and 2(*c*) are unimodal with peaks at $U/V_{bl} = 1.06$ and 7.6, respectively, while the p.d.f. in figure 2(*c*) is bimodal with peaks at $U/V_{bl} = 2$ and 3.1. The dashed vertical lines in figures 2(*a*), 2(*c*) and 2(*e*) show the values of the ratio V_L/V_{bl} of the shear velocity V_L (see (3.2)) and the boundary layer velocity V_{bl} (see (3.3)) at the corresponding Ra_w. We choose V_L as the relevant shear velocity, rather than V_F of (1.1), since V_L is measured closer to the plate at distances of the order of h_m, at which the present velocity fields are measured. The values of V_L and V_{bl} for the range of Ra_w in the present study are listed in table 1.

It needs to be noted that at each Ra_w, all three types of p.d.f.s shown in figure 2 were observed. However, as we discuss in § 3.4, the relative occurrence of these types of p.d.f.s changed with increasing Ra_w. At the lowest $Ra_w = 2.76 \times 10^5$, the p.d.f.s obtained were predominantly (45 %) of a unimodal nature with a peak at $U/V_{bl} \approx 1$, similar to that shown in figure 2(*a*); hereinafter, we refer to these as type A p.d.f.s. The most frequently occurring horizontal velocities at the lowest Ra_w are then of the order of V_{bl}, the NCBL velocity, given by (3.3). The spatial distribution of the velocities corresponding to these type A p.d.f.s, as shown in figure 2(*b*), shows a converging nature towards various randomly oriented lines.

At the highest near-plate Rayleigh number $Ra_w = 6.05 \times 10^8$ also, we observed predominantly (71 %) unimodal p.d.f.s that were, however, peaking mostly at values greater than V_L/V_{bl}, as shown in figure 2(*e*) for a specific instant; hereinafter, we refer to these types of p.d.f.s as type C. The most frequently occurring horizontal velocities at the largest Ra_w are then of the order of, or greater than, V_L. The spatial distribution of velocities shown in figure 2(*f*), corresponding to these type C p.d.f.s, shows a more aligned nature, with larger magnitudes of velocity vectors compared to those with type A p.d.f.s at $Ra_w = 2.76 \times 10^5$ in figure 2(*b*).

In contrast to p.d.f.s at low and high Ra_w, for an intermediate $Ra_w = 1.31 \times 10^7$, we obtain mostly (73 %) p.d.f.s of a bimodal nature. As shown in figure 2(*c*) for a specific instant, the first peaks of these bimodal p.d.f.s occur in between $U/V_{bl} \approx 1$ and V_L/V_{bl}, while the second peaks occur at a value greater than or equal to V_L/V_{bl}. Hereinafter, the bimodal distributions of this form are referred to as type B. Unimodal p.d.f.s are

also observed at these intermediate Ra_w, but at only approximately 21 % of the instants. Most of the unimodal p.d.f.s observed at this intermediate Ra_w peak at $U/V_{bl} > 1 + \frac{2}{3}(V_L/V_{bl} - 1)$ or $U/V_{bl} < 1 + \frac{1}{3}(V_L/V_{bl} - 1)$. Horizontal velocities corresponding to the peaks of the former are much greater in magnitude compared to the velocities corresponding to the peaks of the latter. Further, the former type of p.d.f. is skewed to the left, similar to the p.d.f. shown in figure 2(*e*), while the latter type of p.d.f. is skewed to the right, similar to the p.d.f. shown in figure 2(*a*). For these reasons, we classify these unimodal p.d.f.s as type C and type A, respectively. Less than 1 % of the total number of p.d.f.s at this intermediate Ra_w show a unimodal nature while peaking at $1 + \frac{1}{3}(V_L/V_{bl} - 1) < U/V_{bl} < 1 + \frac{2}{3}(V_L/V_{bl} - 1)$. For this very small number of unimodal p.d.f.s, we consider those peaking at $U/V_{bl} < 1 + \frac{1}{2}(V_L/V_{bl} - 1)$ to be of type A. An instance of such a p.d.f. that occurs at the intermediate $Ra_w = 1.31 \times 10^7$ is shown with the symbol ∘ in figure 2(*a*), which peaks at $U/V_{bl} = 1 + 0.4(V_L/V_{bl} - 1)$. From these 1 % p.d.f.s at intermediate Ra_w, those peaking at $U/V_{bl} > 1 + \frac{1}{2}(V_L/V_{bl} - 1)$ are considered to be of type C; the p.d.f. shown by ∘ in figure 2(*e*) is an example of such a case.

3.2.1. *Effect of Ra_w*

We now present the evolution of p.d.f.s with Ra_w at a fixed Γ. Figure 2(*a*) and its inset show the instantaneous p.d.f.s of the dimensionless horizontal velocity magnitudes at $Ra_w = 2.76 \times 10^5$ and 1.66×10^6 for $\Gamma = 10$. Both of the p.d.f.s are of type A, skewed to the right. With increasing Ra_w, the p.d.f. that peaked at $U/V_{bl} = 1.06$ in figure 2(*a*) peaks at a higher magnitude $U/V_{bl} = 1.31$ in the inset of figure 2(*a*). The horizontal velocity vector field corresponding to the p.d.f. shown in this inset is of a nature similar to that at the lowest $Ra_w = 2.76 \times 10^5$ shown in figure 2(*b*).

Similarly, type C p.d.f.s for $\Gamma = 2$ at $Ra_w = 2.21 \times 10^8$ and 4.04×10^8 are shown in figures 4(*a*) and 4(*b*). Both of these p.d.f.s are skewed to the left, similar to the type C p.d.f. at the highest $Ra_w = 6.05 \times 10^8$, shown in figure 2(*e*). With increasing Ra_w, the p.d.f. that peaked at $U/V_{bl} = 5.73$ in figure 4(*a*) peaks at a higher magnitude $U/V_{bl} = 6.47$ in figure 4(*b*). The horizontal velocity vector fields corresponding to the p.d.f.s shown in figures 4(*a*) and 4(*b*) are of a nature similar to that at the highest $Ra_w = 6.05 \times 10^8$ shown in figure 2(*f*). Clearly, with increasing Ra_w, at a constant aspect ratio, the p.d.f.s of both type A and type C peak at increasing magnitudes of the dimensionless horizontal velocity U/V_{bl}.

3.2.2. *Effect of aspect ratio Γ*

We are unable to study the effect of varying aspect ratio on the p.d.f.s at the same Ra_w since we have not explored such a parameter range in our experiments. However, by comparing three cases of type A p.d.f.s, at $(Ra_w, \Gamma) = (2.76 \times 10^5, 10)$, $(1.66 \times 10^6, 10)$ and $(1.31 \times 10^7, 4.3)$ – shown with ∗ in figure 2(*a*) and its inset, and with ∘ in figure 2(*a*), respectively – we can get an idea of the effect of decreasing Γ. For $\Gamma = 10$, the type A p.d.f., which peaked at $U/V_{bl} = 1.06$ at $Ra_w = 2.76 \times 10^6$ in figure 2(*a*), shifted to peak at $U/V_{bl} = 1.31$ at $Ra_w = 1.66 \times 10^6$ in the inset of figure 2(*a*); the shift in the peak of the p.d.f. was then by 24 % for a change in Ra_w by a factor of six. This type A p.d.f. shifted to peak at $U/V_{bl} = 1.83$ at $Ra_w = 1.31 \times 10^7$ when Γ decreased to 4.3 from 10 in figure 2(*a*); the shift in the peak of the p.d.f. was by 40 % for a change in Ra_w by a

factor of eight. This larger shift of type A p.d.f., compared with the former case at the same Γ, occurred possibly due to the decrease of Γ from 10 at $Ra_w = 1.66 \times 10^6$ to 4.3 at $Ra_w = 1.31 \times 10^7$ in the latter case.

Similar effects of decreasing Γ can also be found on type C p.d.f.s by comparing three cases of type C p.d.f.s at $(Ra_w, \Gamma) = (2 \times 10^7, 4.3)$, $(1.10 \times 10^8, 2.5)$ and $(6.05 \times 10^8, 1.71)$. These cases are shown in the inset of figure 2(*e*) and with the symbols $\circ$ and $*$ in figure 2(*e*), respectively. The p.d.f. at $Ra_w = 2 \times 10^7$, shown in the inset of figure 2(*e*), is skewed to the left, similar to the p.d.f. at $Ra_w = 6.05 \times 10^8$, shown in figure 2(*e*). The velocity field corresponding to the p.d.f. shown in the inset of figure 2(*e*) is similar to that at the highest $Ra_w = 6.05 \times 10^8$ shown in figure 2(*f*). However, the type C p.d.f. that peaked at $U/V_{bl} = 2.7$ at intermediate $Ra_w = 2 \times 10^7$ shifted to peak at $U/V_{bl} = 5.2$ at $Ra_w = 1.10 \times 10^8$, with $\circ$ in figure 2(*e*). The shift in the peak of the p.d.f. was by 93 % for a change in Γ by a factor of 1.7, and in Ra_w by a factor of 5.5. With increase in Ra_w to $Ra_w = 6.05 \times 10^8$ by the same factor of 5.5, the type C p.d.f. shifted to a higher value of $U/V_{bl} = 7.6$, with $*$ in figure 2(*e*). The shift in p.d.f. was by 46 % for a change in Γ by a factor of 1.45, when Ra_w increased by the same factor of 5.5. This larger shift of the p.d.f. when Ra_w increased from 2×10^7 to 1.10×10^8, compared to the case when Ra_w increased by the same factor from 1.10×10^8 to 6.05×10^8, is possibly due to the larger decrease in Γ by a factor of 1.7 in the former case, as against the decrease in Γ by a factor of 1.45 in the latter case. Clearly, these larger shifts in type A and type C peaks to higher magnitudes of the dimensionless horizontal velocity U/V_{bl} are due to the increased cell height H or the decreased Γ.

In summary, the p.d.f.s of the boundary layer velocity field show peaks at velocities of different magnitudes based on the value of Ra_w. At low Ra_w, we obtain unimodal p.d.f.s (type A) that peak at approximately the NCBL velocities V_{bl} (see (3.3)). At high Ra_w, we again obtain unimodal p.d.f.s (type C) that peak predominantly at (or greater than) V_L (see (3.2)), which is the appropriate scale for shear velocities very close to the hot plate. At intermediate Ra_w, the p.d.f.s are bimodal (type B). The first peak of the bimodal distribution occurs at $1 < U/V_{bl} < V_L/V_{bl}$, which we expect to be due to the forcing of the NCBL velocities by the shear due to the LSF; the second peak corresponds to the shear velocities V_L (see (3.2)). A small number of unimodal p.d.f.s that occur at these intermediate Ra_w are classified as type A or type C based on whether their peak is closer to V_{bl} or V_L, respectively.

As mentioned earlier, and discussed in § 3.4, bimodal p.d.f.s are observed at lower Ra_w, as well as at higher Ra_w; the frequency of occurrence of such bimodal p.d.f.s is, however, low at these Ra_w. Further, in such bimodal p.d.f.s observed at lower Ra_w, the likelihood of occurrence of the first peak velocities was much higher than that of the second peak velocities, as shown in figure 3(*a*) at $Ra_w = 1.66 \times 10^6$. In contrast, at the highest $Ra_w = 6.05 \times 10^8$, the bimodal p.d.f.s show the likelihood of occurrence of the second peak velocities to be much higher than that of the first peak velocities, as seen in figure 3(*c*). Hence, comparing the bimodal p.d.f.s at the lower, intermediate and highest Ra_w cases in figures 3(*a*), 2(*c*) and 3(*c*), respectively, we conclude that the likelihood of occurrence of V_{bl} decreases with increase in Ra_w, while that of V_L increases with increase in Ra_w.

As we saw earlier, the velocity fields corresponding to the type A p.d.f.s are oriented randomly (see figure 2*b*), implying absence of significant shear due to the LSF in most regions. In contrast, the velocity field corresponding to type C p.d.f.s, shown in figure 2(*f*), has aligned velocity vectors in most of the domain, implying that the velocity field is

strongly affected by the shear due to the LSF in most of the domain. In the case of bimodal p.d.f.s, we separate the velocity field into two regions at the value of U/V_{bl} at the trough between the two peaks. Figure 2(*d*) shows the regions corresponding to velocities of the first mode as the blue/cyan regions, and the regions corresponding to the velocities of the second mode as red/yellow regions. The velocities in the blue regions are of random nature, similar to the velocities in figure 2(*b*), while those in the red region are of aligned nature, similar to the velocities in figure 2(*f*). The decreasing likelihood of occurrence of V_{bl}, and the corresponding increasing likelihood of occurrence of V_L with increasing Ra_w, seen in the p.d.f.s in figures 3(*a*), 2(*c*) and 3(*c*), can also be clearly seen in the corresponding velocity fields in figures 3(*b*), 2(*d*) and 3(*d*). In these figures, with increase in Ra_w, the areas of the blue/cyan regions, which are mildly affected by shear, decrease, compared to the areas strongly affected by shear, in the red/yellow regions.

3.3. *Area affected by shear*

We now study the evolution of areas of such shear affected regions with Ra_w. At any instant, for bimodal p.d.f.s, we calculate the ratios of areas corresponding to the first mode (A_{bl}) and the second mode (A_{sh}) to the total area (A). In unimodal p.d.f.s of type A and type C, a similar splitting of the total area A into areas strongly affected by shear (A_{sh}) and areas mildly affected by shear (A_{bl}) can be achieved as well, by using appropriate thresholds, as described below. In figure 2(*b*), which is the velocity field corresponding to a p.d.f. of type A shown in figure 2(*a*), the green region around $(-10, 20)$ mm has velocity vectors of aligned nature with velocity magnitudes greater than V_L. The velocity vectors in this region are of a nature similar to that in regions corresponding to the second mode (red/yellow regions in figure 2*d*) in bimodal p.d.f.s, or to those in most of the regions corresponding to type C p.d.f.s (figure 2*f*). Hence when unimodal p.d.f.s of type A occur, we separate the regions strongly affected by shear from the regions mildly affected by shear using a threshold at $U/V_{bl} > V_L/V_{bl}$. Since the velocities below $U/V_{bl} = 1$ are not the shear velocities due to the LSF (see (3.2)), when p.d.f.s of type C occur, we separate the areas mildly affected by shear from the areas strongly affected by shear using the threshold $U/V_{bl} < 1$. In this way, at each Ra_w, we calculate the instantaneous area ratios A_{bl}/A and A_{sh}/A at all the instants, using the appropriate threshold from the above three thresholds, depending upon the type of p.d.f. that occurs at each instant.

Figure 5 shows the variation of $\langle A_{bl}/A\rangle$ and $\langle A_{sh}/A\rangle$ with Ra_w, where $\langle\cdot\rangle$ indicates the mean of the instantaneous area ratios over all the instants at each Ra_w. The values of $\langle A_{bl}/A\rangle$ decrease with increase in Ra_w, while those of $\langle A_{sh}/A\rangle$ increase with increase in Ra_w; increase in Ra_w then increases the areas strongly affected by shear due to the LSF. This increase is drastic in the range $1.66 \times 10^6 \leqslant Ra_w \leqslant 1.10 \times 10^8$, with approximately 20 % of the area strongly affected by shear in the lower limit, changing to 90 % of the area strongly affected by shear in the higher limit; quite small variations are seen in the extent of areas strongly affected by shear beyond this range of Ra_w. The increase of $\langle A_{sh}/A\rangle$ shows a trend opposite to the decrease of $\langle A_{bl}/A\rangle$, as expected, since $\langle A_{bl}/A\rangle + \langle A_{sh}/A\rangle = 1$. As shown in figure 5, the dependence of $\langle A_{sh}/A\rangle$ on Ra_w can be approximated well by

$$\langle A_{sh}/A\rangle = 1 - (a\,\mathrm{e}^{bRa_w} + c\,\mathrm{e}^{dRa_w}), \tag{3.4}$$

where $a = 0.7229$, $b = -0.1416 \times 10^{-7}$, $c = 0.09798$ and $d = -0.5553 \times 10^{-11}$. The relation (3.4) implies that at $Ra_w \approx 10^{12}$, $\langle A_{sh}/A\rangle = 1$; the whole area is then affected by shear. However, this specific limiting value of Ra_w needs to be verified further with measurements at higher Ra_w since (3.4) is not accurate beyond $Ra_w = 6.05 \times 10^8$.

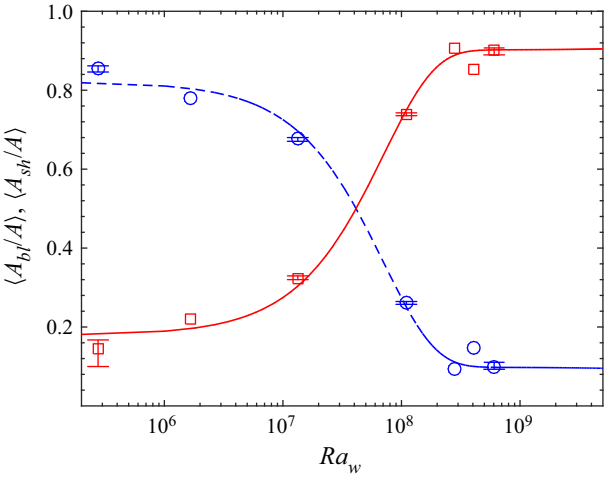

Figure 5. Variation of the mean fraction of areas mildly affected by shear A_{bl}/A, and that of areas strongly affected by shear $\langle A_{sh}/A\rangle$, with Ra_w. Red squares indicate $\langle A_{sh}/A\rangle$; blue circles indicate $\langle A_{bl}/A\rangle$; red solid line uses (3.4); blue dashed line uses (3.5). The error bars show the estimated errors 10.8 % in A_{bl}/A and 31.6 % in A_{sh}/A at $Ra_w = 6.05 \times 10^8$ and 2.76×10^5, respectively. Details of error analysis can be found in Appendix C.

Since $A_{sh} + A_{bl} = A$, the corresponding relation for $\langle A_{bl}/A\rangle$ will be

$$\langle A_{bl}/A\rangle = 1 - \langle A_{sh}/A\rangle, \tag{3.5}$$

with $\langle A_{sh}/A\rangle$ given by (3.4).

3.4. *Number of occurrences of p.d.f.s*

As mentioned earlier, at each Ra_w, all three types of p.d.f.s occur with varying relative occurrences. The percentages of the numbers of type A, B and C p.d.f.s in the total number of p.d.f.s, at each of the five different Ra_w, are shown in figure 6. At the smallest $Ra_w = 2.76 \times 10^5$ in figure 6, the p.d.f.s are mostly type A and type B, with the number of type A p.d.f.s (46 %) being roughly equal to the number of type B p.d.f.s (53 %). The type A p.d.f.s peak at $U/V_{bl} \sim 1$ at this Ra_w (figure 2*a*). Even though type B p.d.f.s are dominant at this Ra_w, since these type B p.d.f.s were similar to that in figure 3(*a*), the probabilities of occurrence of the first peak velocities were much higher than those of the second peak velocities. The velocities at this Ra_w were then mostly of the order of V_{bl} (see (3.3)).

As Ra_w increases from 2.76×10^5 to 1.31×10^7, the percentages of both type B and type C p.d.f.s increase from 53 % to 73 %, and from 1 % to 6 %, respectively, at the expense of type A p.d.f.s, which decrease from 46 % to 21 %. With increase in Ra_w, the first peaks of the type B p.d.f.s shift from $U/V_{bl} \sim 1$ at the lowest Ra_w (figure 3*a*), through $U/V_{bl} \sim 2$ at the intermediate Ra_w (figure 2*c*), to $U/V_{bl} \approx 3$ at higher Ra_w (figure 3*c*). Similarly, the type A p.d.f.s – which peaked at $U/V_{bl} = 1$ at low Ra_w – shift with increase in Ra_w, to peak at $U/V_{bl} = 1.83$, as shown in figure 2(*a*). The local NCBLs, which contribute to the type A p.d.f.s and the first peak of the type B p.d.f.s, could then be changing to a mixed convection type with increase in Ra_w.

Comparing the last three Ra_w in figure 6, we see that the percentage of type C p.d.f.s increases from 6 % to 70 % with increase in Ra_w from 1.31×10^7 to 6.05×10^8, at the expense of both the type A and type B p.d.f.s. Further, as shown in figure 2(*e*), peaks of

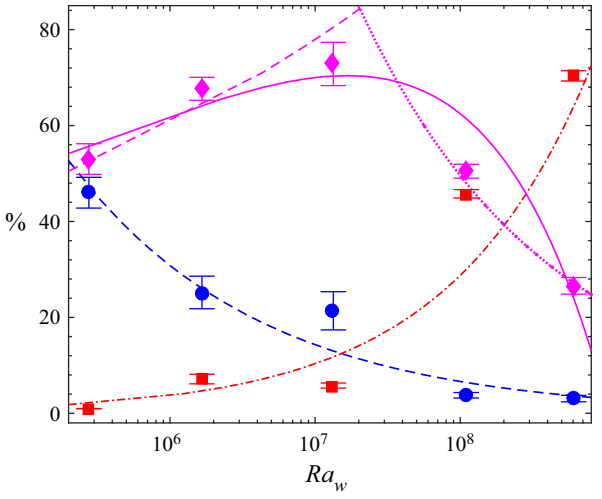

Figure 6. Variation of the percentages of type A, type B and type C p.d.f.s in the total number of p.d.f.s, with Ra_w. The total numbers of p.d.f.s at each Ra_w are given in table 2. Blue circles indicate type A; magenta diamonds indicate type B; red squares indicate type C; blue dashed line for $3080\,Ra_w^{-1/3}$; magenta solid line for $14.8\,Ra_w^{1/9} - 0.0145\,Ra_w^{-4/9}$; red dash-dotted line for $0.008\,Ra_w^{4/9}$; magenta dashed line for $13\,Ra_w^{1/9}$; magenta dotted line for $23\,000\,Ra_w^{-1/3}$. The error bars show the errors 7.1 % in type A p.d.f.s, 18.7 % in type B p.d.f.s, and 23.6 % in type C p.d.f.s, at $Ra_w = 2.76 \times 10^5$. Details of error analysis can be found in Appendix C.

type C p.d.f.s shift from $U/V_{bl} = 5$ at an intermediate $Ra_w = 1.10 \times 10^8$ to $U/V_{bl} = 7.6$ at the highest $Ra_w = 6.05 \times 10^8$. At the highest $Ra_w = 6.05 \times 10^8$, the shear velocities caused by the LSF dominate the boundary layer flow field even though approximately 30 % of the p.d.f.s are still type A and type B, which have their sole/first modes showing mixed convection nature. Figure 5 shows that these mixed convection regions that are mildly affected by shear are limited to approximately 10 % of the area at the highest Ra_w.

We now look at the scaling of percentages of types of p.d.f.s with Ra_w. As shown in figure 6, as Ra_w increases, the percentages of type A peaks decrease from 46 % at $Ra_w = 2.76 \times 10^5$ and become negligible (3 %) at the highest Ra_w. The figure shows that the percentages of type A peaks scale as

$$N_A = 3080\,Ra_w^{-1/3}, \tag{3.6}$$

in the same way as λ_0 (see (1.5)) scales with Ra_w. At the same time, the percentages of type C peaks increase from 1 % at $Ra_w = 2.76 \times 10^5$ and become the highest (70 %) at the highest Ra_w, scaling as

$$N_C = 0.008\,Ra_w^{4/9}, \tag{3.7}$$

in the same way as the shear velocities caused by the LSF V_L (see (3.2)) scale with Ra_w. The variation of percentages of type B peaks with Ra_w is non-monotonic, as shown in figure 6, and can be fitted with a combination of increasing and decreasing power-law functions, of the form

$$N_B = 14.8\,Ra_w^{1/9} - 0.0145\,Ra_w^{-4/9}. \tag{3.8}$$

Interestingly, as shown in figure 6, for the first three Ra_w, this relation has an effective exponent $1/9 = 4/9 - 1/3$, a sum of the power-law exponents of the variations of

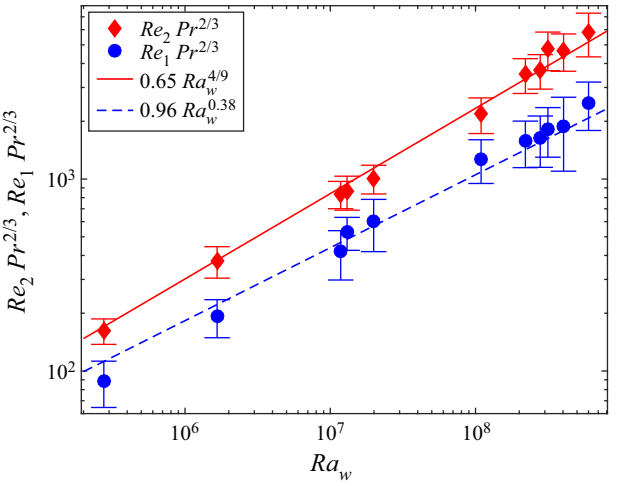

Figure 7. Variation of the mean Reynolds numbers based on the first peak velocities of type B p.d.f.s and the sole peak of the type A p.d.f.s (Re_1), and that based on the second peak velocities of type B p.d.f.s and the sole peak of the type C p.d.f.s (Re_2), with Ra_w.

percentages of type C and type A p.d.f.s, respectively. For the last two Ra_w, the effective power-law exponent for the variation of the percentages of type B p.d.f.s is $-1/3$.

3.5. *Experimental scaling of peak velocities*

At each Ra_w, from various instants, using all the second peaks of the bimodal p.d.f.s of type B, and the sole peaks of the unimodal p.d.f.s of type C, whichever occurs at each instant, we calculate the mean velocity V_2, and the corresponding Reynolds number $Re_2 = V_2 H/\nu$. In estimating V_2, we neglect the instants when type A p.d.f.s occur. Figure 7 shows the variation of Re_2 with Ra_w, along with (3.2), with the error bars showing the 2σ variation of the V_2 values; it is clear that Re_2 scales in the same way as Re_L given by (3.2), with a small increase in the prefactor. Similarly, at each instant, we calculate the mean from the first peak of the bimodal p.d.f.s and the unimodal peak of type A p.d.f.s, whichever occurs at that instant, for each Ra_w. We denote this mean velocity as V_1, with the corresponding Reynolds number as $Re_1 = V_1 H/\nu$; p.d.f.s of type C are skipped in this calculation. Figure 7 shows the variation of Re_1 with Ra_w; interestingly, $Re_1 \sim Ra_w^{0.38}$, the same dependence as that of Nu on Ra_w observed by He *et al.* (2012) at high Ra_w. The variation of Re_1 does not follow the $Ra_w^{1/3}$ scaling of NCBL velocities (3.3), which are expected to occur in the absence of external shear; neither does it follow the scaling of Re_L in (3.2) due to LSF. As we have seen in § 3.2, the peaks of type A p.d.f.s and the first peak of the type B p.d.f.s occur at values larger than V_{bl} with increasing Ra_w, as expected due to the forcing of the boundary layers by the increasing LSF strength. We hence expect the deviation of Re_1 from (3.3) to be due to the shear generated by the LSF changing the characteristic velocities within the boundary layer. Based on this expectation, we now look at the expected theoretical variation of the characteristic velocity within NCBLs when these local boundary layers are forced by the shear due to the LSF velocity V_F.

4. Scaling of boundary layer velocity forced by shear

4.1. *Scaling relation for horizontal velocity*

We consider a two-dimensional laminar NCBL on a horizontal surface, forced by an external shear due to an LSF of strength V_F, as shown in figure 8. The external shear at the edge of the boundary layer is of strength AV_F, where $A = u_{y=\delta}/V_F$ is the dimensionless shear at the edge of the boundary layers. We consider local boundary layers that occur on either side of the plumes on the hot plate, unlike the global, single boundary layer that is considered in many flux scaling theories (Grossmann & Lohse 2000; Ahlers *et al.* 2009; Chilla & Schumacher 2012; Scheel & Schumacher 2017). These local boundary layers are an order thinner than the global boundary layers ($\delta_{nc}/\delta_{pb} = 0.2$ at $Ra = 1.21 \times 10^9$), which, due to their larger thickness, are more likely to be affected by the turbulent bulk. These local boundary layers on the hot plate become unstable to turn upwards and form the plumes. Since plumes are the outcome of the instability of these thin local boundary layers, on either side, it is natural to expect that before they become unstable, these boundary layers will be laminar. Further, successful scaling laws for the mean spacing between such line plumes (Theerthan & Arakeri 1998, 2000; Puthenveettil & Arakeri 2005), their total lengths (Puthenveettil *et al.* 2011) and their mean dynamics (Gunasegarane & Puthenveettil 2014) have all been obtained assuming steady two-dimensional laminar NCBLs (Rotem & Classen 1969; Pera & Gebhart 1973*a*) feeding these plumes. More importantly, the observed vertical distributions of fluctuations of velocities and temperature near the hot plate have been predicted well by a model that assumes laminar boundary layers giving rise to laminar plumes (Theerthan & Arakeri 1998). This means that the observed fluctuations in velocity and temperature near the hot plate are created by the spatial averaging of a spatially non-uniform field consisting of many laminar local boundary layers giving rise to many plumes, as well as by the lateral motion of such plumes (Shevkar & Puthenveettil 2022). Also, as an *a posteriori* justification, the scaling laws obtained in the present study using two-dimensional steady laminar local boundary layer equations, forced by shear, match well with our measurements in turbulent RBC shown later, in figure 10. For these reasons, we expect that our assumption of a laminar mixed convection nature of the local boundary layers that occurs on either side of the plumes on the plate in turbulent convection, which we use to find the scaling of peak velocities in areas mildly affected by shear, to be valid, for at least $Ra \lesssim 10^9$. The integral boundary layer equations

$$\frac{\partial}{\partial x}\int_0^\delta u^2\,\mathrm{d}z - AV_F\frac{\partial}{\partial x}\int_0^\delta u\,\mathrm{d}z - g\beta\int_0^\delta\frac{\partial}{\partial x}\int_0^\delta (T-T_B)\,\mathrm{d}z\,\mathrm{d}z + \nu\left.\frac{\partial u}{\partial z}\right|_{z=0} = 0 \quad (4.1)$$

and

$$\frac{\partial}{\partial x}\int_0^{\delta_T} u(T-T_B)\,\mathrm{d}z + \alpha\left.\frac{\partial T}{\partial z}\right|_{z=0} = 0, \quad (4.2)$$

derived as (A8) and (A13), relate the horizontal velocity and temperature distributions within such boundary layers.

By using the characteristic scale for the driving temperature difference and the scales for the lengths in the horizontal and vertical directions in (4.1) and (4.2), with the external shear given by AV_F, we now obtain scaling relations for U_c, the characteristic horizontal velocities within NCBLs forced by the shear due to the LSF. The characteristic scale of temperature difference in (4.1) and (4.2) is ΔT_w. The vertical length scale in (4.1) is δ, while that in (4.2) is δ_T, as shown in figure 8. Since these boundary layers become unstable

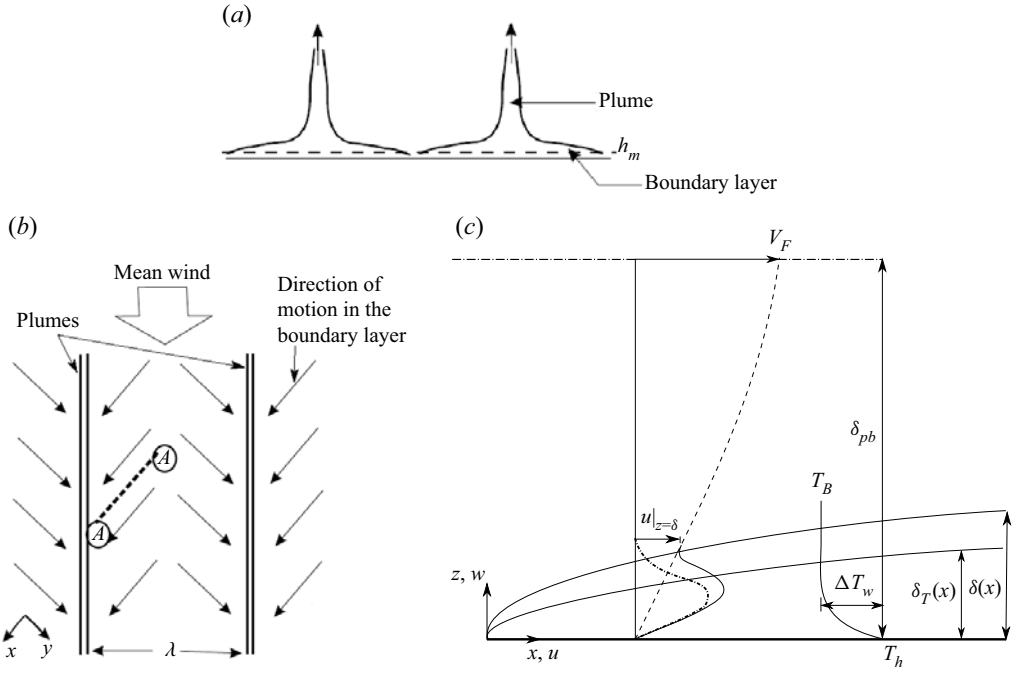

Figure 8. Schematic of the local boundary layer being forced by an external shear due to the LSF for $Pr > 1$: (*a*) side view; (*b*) top view, and (*c*) view along line *A*–*A*. Dash-dotted line indicates horizontal velocity profile within an NCBL; dashed line indicates horizontal velocity profile within a PBBL; solid line indicates horizontal velocity profile due to forcing by external shear of NCBL velocities.

at a horizontal distance to result in line plumes, the appropriate characteristic horizontal distance is half of the mean plume spacing λ, given by (1.6). However, for the present range of Ra_w, the second term in (1.6) becomes at least an order smaller than the first term and can hence be neglected; then $\lambda \approx \lambda_0$. Using these characteristic scales, the order of magnitude balances of (4.1) and (4.2) become

$$\frac{U_c^2\delta}{\lambda_0/2} - \frac{AV_F U_c\delta}{\lambda_0/2} - \frac{g\beta\,\Delta T_w\,\delta^2}{\lambda_0/2} + \frac{\nu U_c}{\delta} \sim 0 \tag{4.3}$$

and

$$\frac{U_c\,\Delta T_w\,\delta_T}{\lambda_0/2} \sim \frac{\alpha\,\Delta T_w}{\delta_T}. \tag{4.4}$$

We now assume

$$\frac{\delta}{\delta_T} = C_2\,Pr^n, \tag{4.5}$$

where C_2 and n are constants. Eliminating δ from (4.3) using (4.5) and (4.4), we obtain the scaling relation for U_c in terms of $Pe_\lambda = U_c\lambda_0/2\alpha$ – the Péclet number based on λ_0 – as

$$8E\,\frac{Pe_\lambda^{5/2}}{Ra_\lambda} - \epsilon\,\frac{4A}{Pr^n}\,Pe_\lambda^{3/2} - C_2 \sim 0, \tag{4.6}$$

where

$$\epsilon = Re_\lambda/Ra_\lambda, \tag{4.7}$$

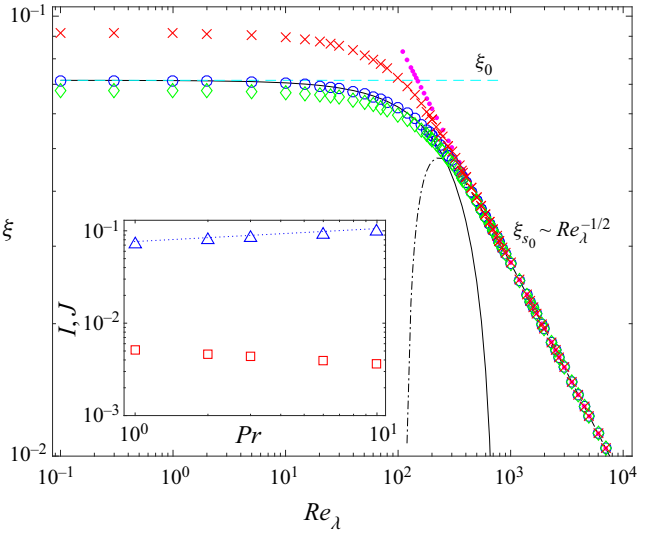

Figure 9. Variation of the critical, local dimensionless boundary layer thickness (4.18) with the shear Reynolds number based on the mean plume spacing (4.8) at $Pr = 1$ and $Ra_\lambda = 1.07 \times 10^5$. Symbols and lines are: blue circles, numerical solution of (4.17); solid black line, (4.22); cyan dashed line, NCBL; magenta dots, PBBL; dash-dotted line, (D5); green diamonds, numerical solution of (4.17) at $Pr = 0.7$ and $Ra_\lambda = 9.63 \times 10^4$; red crosses, numerical solution of (4.17) at $Pr = 6$ and $Ra_\lambda = 1.83 \times 10^5$. The inset shows the variations of I (see (4.26)) and J (see (4.27)) with Pr for $n = 0.5$ and $\Gamma = 1.71$: blue triangles, $I(Pr)$; red squares, $J(Pr)$; blue dotted line, $0.09\,Pr^{0.14}$. In computing solutions of (4.22) and (D5), terms of orders ϵ^2 and ϵ_1^2 were neglected, respectively.

with

$$Re_\lambda = V_F \lambda_0 / \nu \tag{4.8}$$

being the shear Reynolds number based on λ_0, $Ra_\lambda = g\beta\,\Delta T_w\,\lambda_0^3/\nu\alpha$ being the Rayleigh number based on λ_0, and

$$E(Pr) = \frac{C_2^2\,Pr^{2n-1} + 1}{C_2^2\,Pr^{3n}}. \tag{4.9}$$

4.2. *Perturbation solution*

The values of Re_λ, Ra_λ and ϵ for the range of Ra_w in the present study are listed in table 3. With increase in Ra_w, Ra_λ remains of order 10^5, while Re_λ changes by a factor 7 from 30 to 209, so that ϵ increases by an order from 10^{-4} to 10^{-3}; ϵ is then a small parameter. We can then find the solution of (4.6) as a power series in ϵ of the form

$$Pe_\lambda = Pe_{\lambda_0} + \epsilon\,Pe_{\lambda_1} + \epsilon^2\,Pe_{\lambda_2} + O(\epsilon^3). \tag{4.10}$$

Substituting (4.10) in (4.6) and comparing the coefficients of similar powers of ϵ, we obtain

$$Pe_{\lambda_0} = \left(\frac{C_2}{8E}\right)^{2/5} Ra_\lambda^{2/5}, \tag{4.11}$$

$$Pe_{\lambda_1} = \frac{1}{5E\,Pr^n}\,A\,Ra_\lambda \tag{4.12}$$

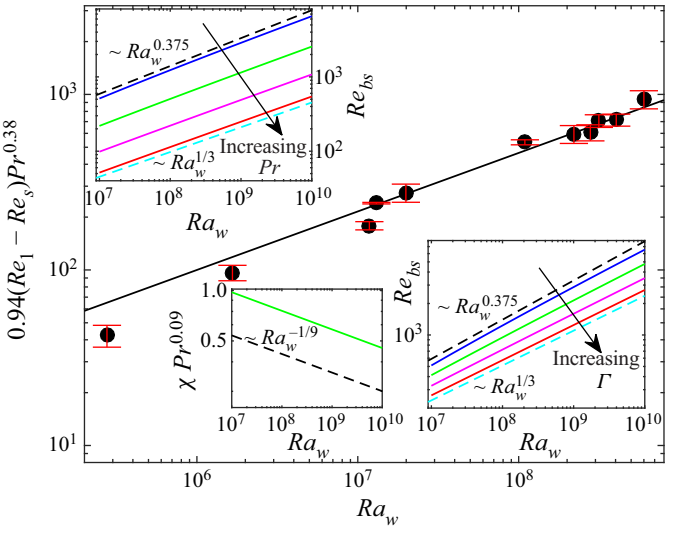

Figure 10. Variation of Reynolds number, based on the mean velocity from the sole peaks of type A p.d.f.s and the first peak of type B p.d.f.s, with Ra_w: black circles, (4.35) with $Re_{bs} = Re_1$; black solid line, $1.0\,Ra_w^{1/3}$. Bottom right inset shows the variation of Re_{bs} (see (4.33)) with Ra_w at $Pr = 1$: blue solid line, $\Gamma = 1$; green solid line, $\Gamma = 2$; magenta solid line, $\Gamma = 5$; red solid line, $\Gamma = 20$; black dashed line, $Ra_w^{0.375}$; cyan dashed line, $Ra_w^{1/3}$. Top left inset shows variation of Re_{bs} (see (4.33)) with Ra_w at $\Gamma = 1$: blue solid line, $Pr = 1$; green solid line, $Pr = 5$; magenta solid line, $Pr = 25$; red solid line, $Pr = 100$; black dashed line, $Ra_w^{0.375}$; cyan dashed line, $Ra_w^{1/3}$. Bottom left inset shows the variation of the dimensionless shear velocity χ (see (4.32)) with Ra_w: green solid line, $\Gamma = 1$; black dashed line, $\Gamma = 10$.

and

$$Pe_{\lambda_2} = \frac{0.069}{C_2^{2/5} E^{8/5}\, Pr^{2n}} A^2\, Ra_\lambda^{8/5}. \tag{4.13}$$

Substituting (4.11)–(4.13) back in (4.10), we obtain

$$Pe_\lambda = \left(\frac{C_2}{8E}\right)^{2/5} Ra_\lambda^{2/5} + \frac{1}{5E\,Pr^n} A\, Re_\lambda + \frac{0.069}{C_2^{2/5} E^{8/5}\, Pr^{2n}} \frac{(A\, Re_\lambda)^2}{Ra_\lambda^{2/5}} + O(\epsilon^3). \tag{4.14}$$

Using (1.5) to replace λ_0 appearing in Re_λ and Ra_λ in (4.14), then using the definitions of Ra_w, Re_{bl}, Re and Z_w, and dropping the second-order terms in Re_λ, we obtain the Reynolds number based on the characteristic velocity in the local NCBL, forced externally by the LSF, as

$$Re_{bs} = \frac{U_c H}{\nu} = \left(\frac{C_2}{E}\right)^{2/5} Re_{bl} + \frac{0.4}{E\,Pr^{n+1}} A\, Re + O(\epsilon^2), \tag{4.15}$$

where Re_{bl} is given by (3.3). Using (1.1) for Re in (4.15) will not capture the effect of Γ on the LSF strength, which is strong in the present case since Γ changes from 10 to 1.71 with increase in Ra in the present experiments. To account for the dependence of Γ on Re, we hence measure the LSF velocity in the present experiments and obtain the corresponding relation (B1) for $Re(Ra, Pr, \Gamma)$ in Appendix B, which is then used in (4.15).

As per (4.15), the velocities in the local boundary layers, in the presence of LSF, are then a linear perturbation of the NCBL velocities by the large-scale velocities, the amount

Ra_w	Re_λ	Ra_λ	$\epsilon = Re_\lambda/Ra_\lambda$
2.76×10^5	29.98	1.82×10^5	1.64×10^{-4}
1.66×10^6	39.18	1.76×10^5	2.23×10^{-4}
1.31×10^7	76.69	1.80×10^5	4.27×10^{-4}
1.10×10^8	137.08	1.76×10^5	7.78×10^{-4}
6.05×10^8	208.62	1.75×10^5	1.19×10^{-3}

Table 3. Values of the Rayleigh and Reynolds numbers based on the mean plume spacing, along with the values of the perturbation parameter for the present study.

of perturbation being dependent on the Pr. This perturbation also depends on the values of shear at the edge of these local boundary layers, given by the dimensionless shear

$$A = \frac{u|_{z=\delta}}{V_F} = 2\,\frac{\delta}{\delta_{pb}} - \left(\frac{\delta}{\delta_{pb}}\right)^2, \tag{4.16}$$

obtained as (A5) in Appendix A, using the von Kármán velocity profile. Since V_F, δ_{pb} and δ in (4.16) are all functions of Ra_w and Pr, A is also a function of Ra_w and Pr. We now find this expression for the dimensionless shear (A) at the edge of the velocity boundary layer. Since A, given by (4.16), is a function of δ, whose dependence on Ra_λ and Re_λ is unknown, we first proceed to find the dependence of δ on Ra_λ and Re_λ.

4.3. *Velocity boundary layer thicknesses for small shear*

Replacing δ_T in (4.4) with δ using (4.5), and substituting the resulting expression for U_c in (4.3), we obtain

$$\frac{4}{C_2^2}\,\xi^5 + 2A\,Pr^{2n}\,\epsilon\xi^2 - \frac{C_2^2\,Pr^{5n}\,E}{Ra_\lambda} \sim 0, \tag{4.17}$$

where

$$\xi = \frac{\delta}{\lambda_0} = \frac{Ra_\delta^{1/3}}{C_1\,Pr^{n_1}} \tag{4.18}$$

is the dimensionless local velocity boundary layer thickness when these boundary layers are perturbed by the LSF, with $Ra_\delta = g\beta\,\Delta T_w\,\delta^3/\nu\alpha$ being the Rayleigh number based on δ and ΔT_w. Let the solution for (4.17) be a power series in ϵ of the form

$$\xi = \xi_0 + \epsilon\xi_1 + O(\epsilon^2). \tag{4.19}$$

Substituting (4.19) in (4.17) and comparing the coefficients of different powers of ϵ, we get

$$\xi_0 = 0.76\,Pr^n \left(\frac{C_2^4 E}{Ra_\lambda}\right)^{1/5} \tag{4.20}$$

and

$$\xi_1 = -0.17A \left(\frac{C_2\,Ra_\lambda}{E}\right)^{2/5}. \tag{4.21}$$

Thus the perturbation solution of (4.17), obtained by substituting (4.20) and (4.21) in (4.19), after neglecting higher-order terms, is

$$\xi \sim 0.76\, Pr^{n} \left(\frac{C_2^4 E}{Ra_\lambda}\right)^{1/5} - 0.17 \left(\frac{C_2}{E}\right)^{2/5} A\, \frac{Re_\lambda}{Ra_\lambda^{3/5}} + O(\epsilon^2). \tag{4.22}$$

Rewriting (4.22) in terms of Ra_δ by using (4.18) and (1.5), we get

$$Ra_\delta^{1/3} = \frac{\delta}{Z_w} \sim 36.1\, Pr^{n+0.1} \left(\frac{C_2^4 E}{Ra_\lambda}\right)^{1/5} - \frac{8.1}{Pr^{-0.1}} \left(\frac{C_2}{E}\right)^{2/5} A\, \frac{Re_\lambda}{Ra_\lambda^{3/5}} + O(\epsilon^2) \tag{4.23}$$

as the expression for the critical, local dimensionless boundary layer thickness, when these boundary layers are forced by an external shear due to the LSF. The first term on the right-hand side of (4.23) is the critical dimensionless boundary layer thickness in the absence of external shear, while the second term is the perturbation due to the external shear. For no external shear, $Re_\lambda \to 0$, $\lambda \to \lambda_0$ and $n = 0.5$ (Puthenveettil *et al.* 2011). Then, using (1.5) and (1.3), for no external shear, (4.23) becomes

$$Ra_\delta \sim 45.1 \left(C_2^4 E\right)^{3/5} Pr^{1.62}, \tag{4.24}$$

which, being constant for a given fluid, is of the same form as the marginal stability condition proposed by Howard (1964).

Figure 9 shows the variation of ξ with Re_λ when $A = 1$ for three different cases $(Pr, Ra_\lambda) = (0.7, 9.63 \times 10^4)$, $(1, 1.07 \times 10^5)$, $(6, 1.83 \times 10^5)$, as given by the numerical solution of (4.17). A similar plot, but for the $Pr = 1$ case alone, was shown by Puthenveettil & Harsha (2010). It needs to be noted that in RBC, Re_λ, Ra_λ and A are all actually interdependent through the LSF, and none of these can be fixed independent of others. Figure 9 could then be considered to show the expected variation of ξ when a small shear is forced externally and independently of the fixed Ra_w, as occurs in the case of mixed convection that causes negligible change of λ from its no-shear value λ_0. Figure 9 also shows the variations predicted by the perturbation solutions (4.22) at $A = 1$ for $(Pr, Ra_\lambda) = (1, 1.07 \times 10^5)$. The perturbation solution (4.22) is a good approximation for the variation of ξ predicted by (4.17) for $Re_\lambda < 250$. The figure shows that for $Re_\lambda < 400$, ξ is a function of Pr and takes larger values for higher Pr; however, ξ becomes a very weak function of Pr for $Re_\lambda > 400$.

For large Re_λ, figure 9 shows that the variation of ξ is similar to that in the Blasius boundary layer. However, at large Re_λ, λ will vary from λ_0 (Shevkar *et al.* 2019), hence the actual variation of ξ will deviate from that shown in figure 9. The singular perturbation solution of (4.17) for large shear, given in Appendix D, shown by the dash-dotted line in figure 9, matches the numerical solution of (4.17) and the variation for PBBLs for large Re_λ. Figure 9 also shows that at $Pr = 1$, the value of ξ decreases by only 10.5 % as Re_λ increases from 10^0 to 10^2, while it decreases by 57 % for further increase in Re_λ from 10^2 to 10^3. Similarly, at $Pr = 6$, the value of ξ decreases by 20 % and 62 % for the increases in Re_λ from 10^0 to 10^2, and from 10^2 to 10^3, respectively. So at any Pr, the deviation of the values of ξ from its natural convection value in (4.20) is less, approximately, for $Re_\lambda \leqslant 100$. For $Re_\lambda > 100$, the value of ξ decreases more rapidly at higher Pr with increase in Re_λ so as to match the variation given by the large shear value ξ_{s_0} (see (D3)), which again is independent of Pr. A similar, larger increase of λ at larger Pr has been found by Shevkar

et al. (2019) at a given Ra_w and Re. Similarly, in sheared convection, with increasing wall shear velocity, Blass *et al.* (2020) found a more pronounced increase of Nu at larger Pr, which could be due to this larger decrease of δ with increasing shear at higher Pr.

For $Re_\lambda < 30$, at any Pr, as shown in figure 9, ξ remains approximately independent of Re_λ, which is the expected variation for a pure NCBL. This constancy of ξ for small shear can be quantified by rewriting (4.22) in terms of Ra_w. Using λ_0 from (1.5) in (4.22), and then using (1.3) and (B1), we obtain

$$\xi \sim I - JA\, Ra_w^{1/9} + O(\epsilon^2), \tag{4.25}$$

where

$$I(Pr) = C_3\, Pr^{n-3/50}\, E^{1/5} \tag{4.26}$$

and

$$J(Pr) = \frac{C_4 \Gamma^{-0.57}}{Pr^{3/4}\, E^{2/5}}, \tag{4.27}$$

with $C_3 = (C_2^4/4C_1^3)^{1/5}$ and $C_4 = 0.27(C_2/C_1^2)^{2/5}$.

For $Pr > 1$, since the velocity boundary layer thickness is more than the thermal boundary layer thickness, in (4.5), n is positive and less than 1 (Shishkina *et al.* 2010); we assume that $n = 0.5$, the same value as in the no-shear case (Puthenveettil *et al.* 2011), for the present case of small shear. The inset of figure 9 shows that for $n = 0.5$, $I(Pr)$ (see (4.26)) is more than an order larger than $J(Pr)$ (see (4.27)). Then since $A < 1$ (see (A5) and figure 8), the second term in (4.25), which has a weak dependence on Ra_w, gives negligible contribution to ξ when $Pr > 1$, for the range of Ra_w in the present study; (4.25) then implies that

$$\xi \sim I(Pr). \tag{4.28}$$

The relation (4.28) implies that in the presence of weak shear, δ and λ_0 have the same functional dependence on Ra_w, so that their ratio is only a function of Pr; a similar dependence occurs in the no-shear case, as has been shown by Puthenveettil *et al.* (2011). As shown in the inset of figure 9, for $n = 0.5$, the rational function (4.26) can be approximated by a simple power law, $I(Pr) \sim Pr^{0.14}$; (4.28) then becomes

$$\xi \sim C_5\, Pr^{0.14}, \tag{4.29}$$

where $C_5 = 0.09$. Rearranging (4.29) using λ_0 from (1.5), we get

$$\frac{\delta}{H} = C_6\, Ra_w^{-1/3}\, Pr^{0.24}, \tag{4.30}$$

where $C_6 = C_1 C_5 = 4.28$. The Pr dependence of δ in (4.30) is the same as that obtained by Lam *et al.* (2002) for the range $6 \leqslant Pr \leqslant 1027$ in RBC.

4.4. *Dimensionless shear (A) at the edge of the boundary layers*

Now that the expression (4.30) for δ, the NCBL thickness forced by small shear, has been obtained, we substitute (4.30) and (1.4) using (B1) in (A5), and simplify, to obtain the

dimensionless shear velocity acting on the edge of the local boundary layers:

$$A = \chi(2-\chi), \tag{4.31}$$

where

$$\chi = \frac{\delta}{\delta_{pb}} = \frac{1.37C_6}{\Gamma^{0.285}\,Ra_w^{1/9}\,Pr^{0.09}}. \tag{4.32}$$

Interestingly, (4.31) and (4.32) show that for a given Γ and Pr, within the limit given by (E4), the dimensionless shear at the edge of the local NCBL decreases with increase in Ra_w as $A \sim (2Ra_w^{1/9} - 1)/Ra_w^{2/9}$. In the present study, since Γ and Ra_w increase much more than the decrease of Pr with increasing Ra_w, A decreases from 0.87 at the lowest Ra_w, to 0.71 at the highest Ra_w. However, the velocity at the edge of these boundary layers, due to the shear by the LSF, is $u|_{y=\delta} = AV_F$ from (A5), where $V_F \sim Ra_w^{4/9}$ from (B1). Hence the actual shear forcing at the edge of these local boundary layers increases with Ra as $u|_{y=\delta} \sim Ra_w^{1/3} - Ra_w^{2/9}$, which has an approximate power-law dependence $Ra^{0.35}$ in the range $10^7 < Ra_w < 10^{10}$. As per the present analysis, since V_{bl} scales as $Ra_w^{1/3}$ (see (3.3)) with increasing Ra_w, the local NCBL would eventually become dominated by shear. However, the present analysis, limited to low shears, does not consider the change in plume spacing due to shear given by (1.6), as well as the change in boundary layer thickness with shear (see (4.30)). The above conclusion of local NCBLs becoming shear-dominant at large Ra_w has to be explored further by extending the present analysis to larger shears by including the changes in the plume spacing and the boundary layer thicknesses at larger shear.

4.5. *Reynolds number based on the characteristic velocity U_c*

We now obtain the effect of external shear caused by the LSF on the velocities within the boundary layers. Substituting (4.31) and (B1) in (4.15), and simplifying, we obtain

$$Re_{bs} = Re_{bl}\left(\left(\frac{C_2}{E}\right)^{2/5} + \frac{F}{\Gamma^{0.855}}(2-\chi)\right) \tag{4.33}$$

as the Reynolds number based on the characteristic velocity close to the hot plate in RBC when the local boundary layers are forced by the LSF. Here,

$$F(Pr) = \frac{0.46\,C_6}{E\,Pr^{1.28}}, \tag{4.34}$$

with χ being given by (4.32), Re_{bl} by (3.3), and E by (4.9), and we have chosen $n = 0.5$ in (4.5), the value in the no-shear case (Puthenveettil *et al.* 2011). Comparing (4.33) and (4.15), we can rewrite (4.33) as

$$Re_{bs} = Re_b + Re_s, \tag{4.35}$$

i.e. the sum of a buoyant contribution and a shear perturbation, where

$$Re_b = \left(\frac{C_2}{E}\right)^{2/5} Re_{bl} = 1.07\,Ra_w^{1/3}\,Pr^{-0.38} \tag{4.36}$$

and

$$Re_s = \frac{0.4}{E\,Pr^{1.5}}\,A\,Re = \frac{1.27}{\Gamma^{0.855}}\,Ra_w^{1/3}\,Pr^{-0.76}\,(2-\chi), \tag{4.37}$$

with Re_{bl}, Re and A given by (3.3), (B1) and (4.31), respectively.

Equation (4.35) gives the variation of the dimensionless boundary layer velocity as a function of Ra_w, Pr and Γ in RBC for small shear by the LSF. The variation predicted by (4.35), shown as the solid line in figure 10, matches the variation of Re_1, the Reynolds number based on the sole peaks of type A p.d.f.s and the first peaks of type B p.d.f.s for a reasonable value $C_2 = 0.72$. The single-peak type A p.d.f.s occurred at the low shear at low Ra_w, while the first peaks of type B p.d.f.s were due to the low-shear regions at all Ra_w. The deviation of the data point at the lowest Ra_w in figure 10 is expected to occur since (1.4) may not be valid for $Ra_w < 10^7$.

It is interesting to see the effective power-law dependence of Re_{bs} on Ra_w corresponding to (4.35). The top left inset of figure 10 shows the variation of Re_{bs} with Ra_w given by (4.35) at $\Gamma = 1$ for $1 \leqslant Pr \leqslant 100$. At $Pr = 1$, a power law $Re_{bs} \sim Ra_w^{0.375}$ approximates (4.35) for $10^7 \leqslant Ra_w \leqslant 3.3 \times 10^8$. As Pr is increased from 1 to 100, the exponent of Ra_w is decreased from 0.375 to $1/3$; Re_{bs} then scales with Ra_w in the same way as Re_{bl} scales with Ra_w (see (3.3)). Therefore, the present analysis suggests that for $Pr \geqslant 100$, the effect of external forcing on the local NCBLs become negligible close to the hot plate. Similarly, the bottom right inset of figure 10 shows that with increase in Γ, the dependence of Re_{bs} on Ra_w becomes weaker, and for $\Gamma \geqslant 20$, $Re_{bs} \sim Ra_w^{1/3}$. It is interesting to note that at $Pr = 1$ and $\Gamma = 1$, Re_{bs} shows the same power law of Nu versus Ra_w observed at large Ra_w (He *et al.* 2012), which has been proposed as a sign of the ultimate regime, even though this inference has been disputed by Urban *et al.* (2012). Considering that at low Ra_w, the scaling of Re_b in (4.36) (or Re_{bl} in (3.3)) with Ra_w is the same as that of Nu with Ra_w, the power-law exponent 0.375 for the dependence of Re_{bs} on Ra_w at higher Ra_w is analogous to what occurs at low Ra_w; the reason for such an interesting occurrence needs to be investigated.

5. Conclusions

The primary contributions of the present work include the novel observations of the three types of horizontal velocity p.d.f.s within the boundary layers, their evolution with Rayleigh numbers (Ra), the evolution of the area affected by shear with Ra, and the novel scaling relations for the dominant horizontal velocities within the boundary layers. Together, these illustrate the effect of external forcing by the large-scale flow (LSF) – which we showed to be a function of Ra, Pr and the aspect ratio Γ (see (B1)) – on the boundary layers on the plate in turbulent Rayleigh–Bénard convection (RBC).

At lower Ra ($\sim 10^6$), in a horizontal plane close to the hot plate, we observed predominantly (figure 2*a*) unimodal, type A p.d.f.s of horizontal velocity magnitudes (U) that had a peak at approximately the natural convection boundary layer (NCBL) velocities (V_{bl}) (see (3.3)). At higher Ra ($\sim 10^9$), these evolved into predominantly unimodal type C p.d.f.s (figure 2*e*), with a velocity peak at approximately double the value of V_L (see (3.2)), the LSF velocity at the edge of the boundary layers. This shifting of p.d.f.s with increase in Ra was also accompanied by more-aligned and larger-magnitude velocity vector fields (figures 2*b*,*f*). Not only the type of p.d.f.s but also their relative occurrences shifted with increasing Ra; the occurrence of type A p.d.f.s decreased from approximately 50 % of instants at low Ra to approximately 10 % of instants at high Ra, while the occurrence of type C p.d.f.s increased from approximately 1 % to 70 % of the instants (figure 6). Interestingly, this change in percentage occurrences of type A and type C p.d.f.s followed a dependence of $Ra^{-1/3}$ (see (3.6)) and $Ra^{4/9}$ (see (3.7)), respectively; the magnitude of

the exponents was the same as those in the classical flux scaling and the scaling of the Reynolds number (Re) (see (1.1)) based on the LSF, respectively.

This shift in types and numbers of p.d.f.s occurred through a stage at intermediate Ra where the p.d.f.s were predominantly bimodal (figure 2*c*). The numbers of these type B p.d.f.s increased from approximately 50 % of instants at low Ra to approximately 70 % of instants at $Ra \approx 10^7$, before decreasing to approximately 25 % of instants at $Ra \approx 10^9$ (figure 6). The first mode of these bimodal type B p.d.f.s peaked at velocities slightly larger than V_{bl}, while the second mode peaked at V_L (figure 2*c*); the regions contributing to the second mode had more aligned velocity fields with larger magnitudes (figure 2*d*). Considering the regions that had aligned velocity vectors with larger magnitudes as shear-affected – which occurred in regions contributing to the second mode in type B p.d.f.s, in regions with $U > V_L$ for type A p.d.f.s, and regions with $U > V_{bl}$ for type C p.d.f.s – we obtained the variation of shear-affected areas with Ra (figure 5). The shear-affected areas increased exponentially with Ra, from approximately 20 % at $Ra = 10^6$, before saturating at approximately 90 % at $Ra = 10^9$; the proposed scaling law (3.4) for this variation matched the observed variation. Thus we showed that the effects of increasing shear, due to increasing LSF strength with Ra, on the boundary layers on the plate occur in the following three simultaneous manifestations: (*a*) change of velocity p.d.f.s, from the ones that peaked at V_{bl} to those that peaked at velocities $\geqslant V_L$; (*b*) an increase in the occurrence of such p.d.f.s that peaked at $\geqslant V_L$; and (*c*) an exponential increase, and then saturation, of the extent of areas affected by shear, that had aligned velocity vectors with larger magnitudes.

In the regions where the effect of shear was felt strongly, i.e. in those regions that had aligned velocity vectors with larger magnitudes, the scaling of velocities – estimated as the scaling of the peaks of type C p.d.f.s and the second mode of the type B p.d.f.s – followed the scaling of V_L. The magnitudes of these velocities (V_2) were, however, larger than V_L, but smaller than V_F, the LSF velocity far away from the plate. In contrast, in regions mildly affected by shear that did not have aligned velocity vectors with larger magnitudes, the scaling of velocities – estimated as the scaling of the peaks of type A p.d.f.s and the peaks of the first mode of type B p.d.f.s – followed neither the scaling of V_{bl} nor that of V_L. Instead, here, the velocities followed $Ra^{0.38}$, the same dependence of flux observed by He *et al.* (2012), suggested as a sign of the ultimate regime. Since the peak of the velocity p.d.f.s from these regions shifted to larger velocities with increase in Ra, and since the scaling anyway was different from that of V_{bl}, we proposed this $Ra^{0.38}$ scaling to be due to the effect of shear by the LSF on the local NCBLs.

Using an order of magnitude balance of integral equations for NCBLs forced by small external shear, (A8) and (A13), we then quantified this effect of shear on the local boundary layers by obtaining a scaling relation (4.6) for the characteristic velocity (U_c) within such boundary layers. Here, the boundary layers were assumed to be embedded within a Prandtl–Blasius boundary layer (PBBL) that had a von Kármán velocity profile (A4), and the plume spacings (1.5) assumed to be unchanged due to the small shear. The perturbation solution of this scaling relation showed that U_c is a sum of V_{bl} and $u|_{y=\delta}$, the shear at the edge of these local boundary layers, with functions of Pr as prefactors on each term of the sum (4.15). The effect of shear was then a linear perturbation of the natural convection velocities by the LSF velocities, with the amount of perturbation being dependent on Pr and the shear $u|_{y=\delta}$ at the edge of the boundary layers.

Since $u|_{y=\delta}$ was dependent on the velocity boundary layer thickness δ of these local boundary layers in the presence of external shear, we obtained a scaling relation (4.22),

$\delta = f_1 Z_w + f_2 Z_w^2/Z_{sh}$, where f_1 and f_2 are functions of Pr, Z_w is the natural convection length scale near the plate (see (1.3)), and $Z_{sh} = \nu/u|_{y=\delta}$ is the viscous shear length at $y = \delta$. At the low shears considered in the present study, the second term in the above relation for δ could be dropped so that δ became the same as the velocity boundary layer thickness of NCBLs in the absence of shear. Using this asymptotic form of δ, we obtained $u|_{y=\delta}$, which scaled as $Ra_w^{1/3} - Ra_w^{2/9}$, with an equivalent power law or $Ra_w^{0.35}$. Then, since $V_{bl} \sim Ra_w^{1/3}$, with increase in Ra_w, we proposed that these local NCBLs are expected to become shear-dominated at some large Ra_w, even though only an analysis that includes the effect of shear on δ and plume spacing, at larger shear, can confirm this expectation. Using this $u|_{y=\delta}$ in the perturbation solution for U_c gave the characteristic Reynolds number Re_{bs} within these boundary layers as a sum of buoyant contribution and shear perturbation (see (4.35)). The relation (4.35) for Re_{bs} – obtained using the derived relations for the shear at the edge of the local boundary layers (4.31) and the local velocity boundary layer thickness subjected to small shear (4.30) – matched the measurements of Reynolds number Re_1 based on the peaks of type A p.d.f.s and the first peak of type B p.d.f.s of horizontal velocity magnitudes (figure 10), obtained from stereo PIV in a plane close to the hot plate. Similarly, the relations for the areas affected by shear (3.4) and the number of occurrences of various types of p.d.f.s (3.6)–(3.8) also matched our experimental observations for $2.76 \times 10^5 \leqslant Ra_w \leqslant 6.05 \times 10^8$, $4.69 \leqslant Pr \leqslant 5.88$ and $1.71 \leqslant \Gamma \leqslant 10$, thereby validating all these relations in this range of parameters.

These relations and the associated experimental observations help us to understand the varied effects of shear due to LSF on the local boundary layers on the hot plate. The scaling (4.35), obtained for the velocities in the mildly shear-affected regions in the boundary layers, appears to contribute progressively less with increase in Ra, in terms of the areas in which they occur, as well as in their number of occurrences. However, this could be because with a horizontal plane of measurement at a fixed height h_m, more areas of the boundary layers, which become progressively thinner with increase in Ra, will evade the measurement plane, as could be inferred from figure 8(*a*). In such a situation, the high-shear regions that show a velocity scaling the same as V_L could actually be outside the local boundary layers, with (4.35) being the scaling in all boundary layers. In such a scenario, the scaling (4.35) could be the key relation showing the effect of shear by LSF on the boundary layers on the hot plate. Application of (4.35) in that case, we hope, will lead to explanations for the anomalous flux scaling in turbulent convection, as well as clarifying the question of the ultimate regime. However, in obtaining these relations, we neglected the effect of shear due to the LSF on the plume spacings and the local boundary layer thicknesses; the present relations will then be valid only for the case of small shear, i.e. $Ra_w < 5.5 \times 10^{11}$ (see Appendix E). To explain the anomalous flux scaling from these effects, we need to extend the present analysis to higher Ra by including these neglected effects.

Funding. The authors gratefully acknowledge the financial support of DST, Government of India through their FIST grants SR/FST/ETII-017/2003, SR/FST/ETII-064/2015 and their core research grants SR/S3/MERC/028/2009 and CRG/2021/007497.

Declaration of interests. The authors report no conflict of interest.

Author ORCIDs.
Prafulla P. Shevkar https://orcid.org/0000-0001-8259-4903;
Baburaj A. Puthenveettil https://orcid.org/0000-0002-8694-4322.

Appendix A. Integral boundary layer equations

The integral x-momentum equation is

$$\int_0^\delta u\,\frac{\partial u}{\partial x}\,\mathrm{d}z + \int_0^\delta w\,\frac{\partial u}{\partial z}\,\mathrm{d}z = -\frac{1}{\rho}\int_0^\delta \frac{\partial p}{\partial x}\,\mathrm{d}z + \nu\int_0^\delta \frac{\partial^2 u}{\partial z^2}\,\mathrm{d}z, \tag{A1}$$

where $\delta(x)$ is the velocity boundary layer thickness, and $p(x, z)$ is the pressure within the boundary layer. Rewriting the second term in (A1) as $\int_0^\delta(\partial(wu)/\partial z - u\,\partial w/\partial z)\,\mathrm{d}z$, integrating, replacing $\partial w/\partial z = -\partial u/\partial x$ from continuity, noticing that $\int_0^\delta(u\,\partial u/\partial x)\,\mathrm{d}z = \int_0^\delta(\partial u^2/\partial x)\,\mathrm{d}z/2$, and since $(\partial u/\partial z)|_{z=\delta} \approx 0$ for small external shear, we obtain

$$\int_0^\delta \frac{\partial}{\partial x}u^2\,\mathrm{d}z + (wu)|_{z=\delta} = \frac{-1}{\rho}\int_0^\delta \frac{\partial p}{\partial x}\,\mathrm{d}z - \nu\left.\frac{\partial u}{\partial z}\right|_{z=0}. \tag{A2}$$

The vertical velocity at the boundary layer edge in the second term in (A2) can be obtained by integrating the continuity equation and applying the Leibniz rule as

$$w|_{z=\delta} = -\frac{\partial}{\partial x}\int_0^\delta u\,\mathrm{d}z + u|_{z=\delta}\,\frac{\partial \delta}{\partial x}. \tag{A3}$$

To obtain $u|_{z=\delta}$ in (A2) and (A3), as shown in figure 8, we assume that the local boundary layers are embedded within a PBBL, which is driven by the LSF strength of V_F, acting at distance δ_{pb} (see (1.4)) from the hot plate. Using the von Kármán velocity profile

$$\frac{u(z)}{V_F} = 2\,\frac{z}{\delta_{pb}} - \left(\frac{z}{\delta_{pb}}\right)^2 \tag{A4}$$

for the PBBL, the dimensionless shear velocity acting on the upper edges of the local NCBLs, at height $z = \delta$ from the hot plate, is then

$$A = \frac{u|_{z=\delta}}{V_F} = 2\,\frac{\delta}{\delta_{pb}} - \left(\frac{\delta}{\delta_{pb}}\right)^2. \tag{A5}$$

Applying the Leibniz rule to the first term in (A2), substituting (A3) in (A2), simplifying, and finally replacing $u|_{z=\delta}$ from (A5), we obtain

$$\frac{\partial}{\partial x}\int_0^\delta u^2\,\mathrm{d}z - AV_F\,\frac{\partial}{\partial x}\int_0^\delta u\,\mathrm{d}z + \frac{1}{\rho}\int_0^\delta \frac{\partial p}{\partial x}\,\mathrm{d}z + \nu\left.\frac{\partial u}{\partial z}\right|_{z=0} = 0. \tag{A6}$$

To replace the unknown pressure in (A6), we integrate the z-momentum equation, $\partial p/\partial z = \rho g\beta(T - T_B)$, to obtain,

$$p = -\rho g\beta\int_0^\delta (T - T_B)\,\mathrm{d}z, \tag{A7}$$

where $T(z)$ is the temperature distribution within the boundary layer. Substituting (A7) in (A6), we obtain

$$\frac{\partial}{\partial x}\int_0^\delta u^2\,\mathrm{d}z - AV_F\,\frac{\partial}{\partial x}\int_0^\delta u\,\mathrm{d}z - g\beta\int_0^\delta \frac{\partial}{\partial x}\int_0^\delta (T - T_B)\,\mathrm{d}z\,\mathrm{d}z + \nu\left.\frac{\partial u}{\partial z}\right|_{z=0} = 0 \tag{A8}$$

as the integral momentum balance equation for the local NCBLs, forced externally by the LSF.

The integral energy equation is

$$\int_0^{\delta_T} u\,\frac{\partial T}{\partial x}\,\mathrm{d}z + \int_0^{\delta_T} w\,\frac{\partial T}{\partial z}\,\mathrm{d}z = \alpha \int_0^{\delta_T} \frac{\partial^2 T}{\partial z^2}\,\mathrm{d}z, \tag{A9}$$

where $\delta_T(x)$ is the thermal boundary layer thickness of the local boundary layer. The first term in (A9) can be written as $\int_0^{\delta_T}(\partial(uT)/\partial x)\,\mathrm{d}z - \int_0^{\delta_T} T(\partial u/\partial x)\,\mathrm{d}z$. Applying the Leibniz rule to the first term in this equation, the first term in (A9) becomes

$$\frac{\partial}{\partial x}\int_0^{\delta_T} uT\,\mathrm{d}z - (uT)|_{z=\delta_T}\,\frac{\mathrm{d}\delta_T}{\mathrm{d}x} - \int_0^{\delta_T} T\,\frac{\partial u}{\partial x}\,\mathrm{d}z. \tag{A10}$$

Similarly, rewriting the second term in (A9) as $\int_0^{\delta_T}(\partial(wT)/\partial z)\,\mathrm{d}z - \int_0^{\delta_T} T(\partial w/\partial z)\,\mathrm{d}z$, integrating the first term and using the continuity equation on the second term, the second term in (A9) becomes

$$(wT)|_{z=\delta_T} + \int_0^{\delta_T} T\,\frac{\partial u}{\partial x}\,\mathrm{d}z. \tag{A11}$$

Replacing $w|_{z=\delta_T}$ in (A11) by $-(\partial/\partial x)\int_0^{\delta_T} u\,\mathrm{d}z + u|_{z=\delta_T}(\mathrm{d}\delta_T/\mathrm{d}x)$ obtained by integrating the continuity equation across the thermal boundary layer and applying the Leibniz rule, similar to (A3), the second term in (A9) becomes

$$-\frac{\partial}{\partial x}\int_0^{\delta_T} uT_B\,\mathrm{d}z + u|_{z=\delta_T}\,T_B\,\frac{\mathrm{d}\delta_T}{\mathrm{d}x} + \int_0^{\delta_T} T\,\frac{\partial u}{\partial x}. \tag{A12}$$

Substituting (A10) and (A12) in (A9) and simplifying, and since the last term in (A9) becomes $-\alpha\,\partial T/\partial z|_{z=0}$ since $\partial T/\partial z|_{z=\delta} \approx 0$, we obtain

$$\frac{\partial}{\partial x}\int_0^{\delta_T} u(T - T_B)\,\mathrm{d}z = -\alpha\,\left.\frac{\partial T}{\partial z}\right|_{z=0} \tag{A13}$$

as the integral energy equation for the local NCBL forced by the LSF.

Appendix B. Dependence of LSF velocities on aspect ratio ($\Gamma = L/H$)

For $Ra \leqslant 10^{13}$, the dependence of the Reynolds number based on the LSF velocities (Re) on Ra and Pr has been well studied. Most studies find $Re \sim Ra^a\,Pr^b$, where $a \approx 4/9$ and $b \approx -2/3$ (Lam *et al.* 2002; Puthenveettil & Arakeri 2005; Ahlers *et al.* 2009; He *et al.* 2012; Gunasegarane & Puthenveettil 2014). However, the magnitude of the LSF velocities and the number of rolls are correlated to each other, and are also dependent on the aspect ratio Γ (Cuba, Emran & Schumacher 2010; Shi *et al.* 2012); this dependence of Re on Γ is not clear. In the present experiments, since Ra was changed by changing H, while keeping L constant, Γ decreased with increasing Ra; $\Gamma = 10$ at the lowest Ra, while at the highest Ra, $\Gamma = 1.71$. Since the variation of Γ is significant in the present experiments, we now find the dependence of Re on Γ in our experiments.

From PIV, we obtain the velocity fields at various instants in horizontal planes at heights $h_F \gtrsim \delta_{pb}$, given in table 1, at six different Ra. At each of these Ra, we calculate the spatio-temporal average of these horizontal velocities to obtain the LSF velocity $V_F = \langle \bar{U} \rangle$. Figure 11 shows the variation of $Re = V_F H/\nu$ with Ra for $1.71 \leqslant \Gamma \leqslant 10$ and $4.69 < Pr < 5.88$. The data show a power-law scaling $Re \sim Ra^{0.617}$, giving the

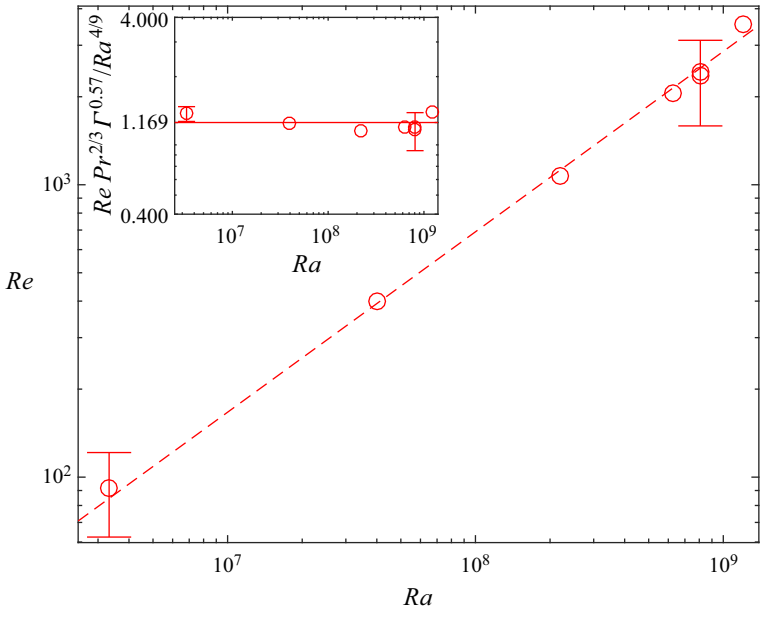

Figure 11. Variation of Reynolds number Re based on V_F with Ra for $1.71 \leqslant \Gamma \leqslant 10$: red dashed line, $0.008\,Ra^{0.617}$. The inset shows the variation of normalised Re with Ra: red solid line, $Re\,Pr^{2/3}\,\Gamma^{0.57}/Ra^{4/9} = 1.169$. Error bars show the 2σ variation of the V_F values.

impression that the dependences of Re on Pr and Γ are weak. However, this could be because of the opposite dependence of Re on Γ and Ra. Further, the range of our Pr is small, so the dependence of Re on Pr may also not be clearly seen. Since it is known that $Re \sim Ra^{4/9}\,Pr^{-2/3}$, as shown in the inset in figure 11 we plot the variation of $Re\,Pr^{2/3}\,\Gamma^m/Ra^{4/9}$ with Ra and find the value $m = 0.57$ that collapses the normalised Re onto a horizontal line. Then the Reynolds number based on the LSF velocities (V_F) and H scales as

$$Re = 1.169\,Ra^{4/9}\,Pr^{-2/3}\,\Gamma^{-0.57}. \tag{B1}$$

Recent RBC experiments by Zhu & Zhou (2021) for $1 \leqslant \Gamma \leqslant 4$, $4.8 \times 10^7 \leqslant Ra \leqslant 4.5 \times 10^{10}$ and $4.3 \leqslant Pr \leqslant 5.3$ found that $Re \sim \Gamma^{-0.52}$, the exponent of Γ being close to that in (B1). The prefactor in (B1) is also very close to the prefactor 1.1 in the expression for Re based on the oscillation frequency of the LSF, obtained by Lam *et al.* (2002). From (1.4) and (B1), it then follows that $\delta_{pb}/H \sim \Gamma^{0.285}$; interestingly, the exponent 0.285 is the same as that in $\delta_t/H \sim \Gamma^{0.29}$, obtained by du Puits, Resagk & Thess (2013) for the scaling of thermal boundary layer thickness, for $1 \leqslant \Gamma \leqslant 9$ at $Pr = 0.7$. Hence the new scaling of Re given by (B1), which is valid for the range of Ra, Pr and Γ in the present experiments, is consistent with the available results.

Niemela & Sreenivasan (2003) observe that V_F/V_{FF} increases until $Ra \approx 10^8$ and then decreases until $Ra = 10^{13}$ in a cylindrical convection cell, where $V_{FF} = \sqrt{g\beta\,\Delta T\,H}$ is the free fall velocity. If we rewrite (B1) in terms of V_{FF}, then $V_F/V_{FF} = 1.169\,Ra^{-1/18}\,Pr^{-1/6}$, which decreases monotonically with Ra. This difference is most likely due to the difference in the shape of the cross-section of the convection cell in the two studies, compounded by the method by which V_F was measured in Niemela & Sreenivasan (2003). In a cylindrical

cell, the orientation of the large scale circulation (LSC) is constantly changing (Chilla & Schumacher 2012), while in a rectangular cell, the LSC is mostly oriented along the diagonal of the cross-section (Vishnu, De & Mishra 2020). Niemela & Sreenivasan (2003) used the correlation between two nearby temperature sensors to estimate the strength of the LSC. In the presence of the LSC that changes its orientation constantly, such an estimate would be accurate if the temperature sensors are aligned in the direction of the LSC, which would happen only for short time periods. Further, their measurements are made at a single point; however, the strength of the LSC does vary spatially. In contrast, our measurements are spatio-temporal averages of direct PIV measurements, which takes into account spatio-temporal non-uniformities as well as well as change in orientation of the LSC. We hence expect our measurements to be a more realistic, accurate and valid estimate in the present set-up.

Appendix C. Error analysis

Errors in U/V_{bl}, at three points of different magnitudes of U/V_{bl}, in type A, type B and type C p.d.f.s, are shown in figures 2 and 3. Uncertainty in U/V_{bl} was assumed to be due to uncertainty in U. Uncertainty in U in a PIV interrogation window was calculated from the correlation statistics using the methodology of Wieneke (2015), using the Davis software (LaVision GmbH). In any p.d.f., the uncertainty at a specific magnitude of U is chosen as the uncertainty in horizontal velocity at any randomly chosen point of the vector field that has the same magnitude as U. The error bars on either side of any point on the p.d.f. are then plotted using half the total error in U/V_{bl}, and are shown either on or just above the points. Then at any point on the p.d.f., an error bar shows a 68.3 % confidence level range in U/V_{bl}. The typical values of uncertainties in U/V_{bl} at $U/V_{bl} = 0.33, 1.06, 3$ in a type A p.d.f. at $Ra_w = 2.76 \times 10^5$ were 7.1 %, 4.9 % and 1.2 %, respectively, as shown in figure 2(*a*). The maximum uncertainty in U/V_{bl} in type A p.d.f.s was 7.1 %, in type B p.d.f.s was 4.9 %, and in type C p.d.f.s was 7 %.

In figure 5, errors in A_{bl}/A and A_{sh}/A at $Ra_w = 2.76 \times 10^5$, 1.31×10^7, 1.10×10^8 and 6.05×10^8 are plotted. As described in § 3.1, the values of A_{bl}/A and A_{sh}/A were calculated at various Ra_w using peak separation value $\frac{1}{4}(V_{sh}/V_{bl} - 1)$. To estimate the errors in A_{bl}/A or A_{sh}/A, the ranges of the variation of the values of A_{bl}/A and A_{sh}/A at any Ra_w are now estimated using peak separation values $0.3(V_{sh}/V_{bl} - 1)$ and $0.2(V_{sh}/V_{bl} - 1)$. The lower limit $0.2(V_{sh}/V_{bl} - 1)$ was chosen, since values lower than this limit picked up peaks due to fluctuations present in turbulent flow, which do not represent the dominant motions in the flow. Similarly, values greater than the upper limit $0.3(V_{sh}/V_{bl} - 1)$ gave unimodal p.d.f.s, and hence were not considered. At any Ra_w, the changes in mean peak velocities V_1 and V_2 at these limits were less than 2 % from that obtained using the peak separation value $\frac{1}{4}(V_{sh}/V_{bl} - 1)$. At a given Ra_w, these ranges of values of A_{bl}/A or A_{sh}/A were used as the errors at the corresponding points. The estimated errors in A_{bl}/A were 0.9 % and 10.8 % at $Ra_w = 2.76 \times 10^5$ and 6.05×10^8, respectively, while the errors in A_{sh}/A were 31.6 % and 1.2 % at $Ra_w = 2.76 \times 10^5$ and 6.05×10^8, respectively.

We now estimate the errors in percentages of type A, type B and type C p.d.f.s by estimating the numbers of these types of p.d.f.s that are obtained by using a range of peak separation values at $Ra_w = 2.76 \times 10^5$, 1.66×10^6, 1.31×10^7, 1.10×10^8 and 6.05×10^8. The percentages of type A, type B and type C p.d.f.s, in figure 6 were estimated using peak separation value $\frac{1}{4}(V_{sh}/V_{bl} - 1)$. To estimate errors, peak separation values

Ra_w	Type A	Type B	Type C
2.76×10^5	7.1	18.7	23.6
1.31×10^7	6.1	6.4	7.4
6.05×10^8	5	12.9	1.7

Table 4. Percentage errors in total number of p.d.f.s at each Ra_w.

$0.2(V_{sh}/V_{bl} - 1)$ and $0.3(V_{sh}/V_{bl} - 1)$ are now used to obtain the percentages of type A, type B and type C p.d.f.s at each Ra_w. The differences between these percentages of each type of p.d.f. are taken as the errors in the percentages of each type of p.d.f. at the corresponding Ra_w. The obtained errors in the percentages of the three types of p.d.f.s at three Ra_w are shown in table 4. Larger errors are observed at lower Ra due to the larger spatial non-uniformity of the velocity field, due to lower velocity strength of LSF.

Appendix D. Velocity boundary layer thickness for large shear

For large shear, using a new perturbation parameter $\epsilon_1 = Ra_\lambda/Re_\lambda = 1/\epsilon$, where ϵ is given by (4.7), assuming that $\lambda \sim \lambda_0$ remains valid, and following the same procedure as in § 4.1, we obtain from (4.17) that

$$\epsilon_1 \xi^5 + \frac{C_2^2 A}{2} Pr^{2n} \xi^2 - \frac{C_2^4 Pr^{5n} E}{4 Re_\lambda} \sim 0. \tag{D1}$$

Let the solution for (D1) be a power series in ϵ_1 of the form

$$\xi = \xi_{s_0} + \epsilon_1 \xi_{s_1} + O(\epsilon_1^2). \tag{D2}$$

Substituting (D2) in (D1) and comparing the coefficients of different powers of ϵ_1, we get

$$\xi_{s_0} = \frac{0.707\, Pr^{3n/2}}{A^{1/2}} \sqrt{\frac{C_2^2 E}{Re_\lambda}} \tag{D3}$$

and

$$\xi_{s_1} = -\frac{Pr^{4n}}{4A^3} \frac{C_2^2 E^2}{Re_\lambda^2}. \tag{D4}$$

Thus the perturbation solution of (D1), obtained by substituting (D3) and (D4) in (D2), after neglecting higher-order terms, is

$$\xi \sim \frac{0.707}{A^{1/2}} \left(\frac{C_2^2 Pr^{3n} E}{Re_\lambda} \right)^{1/2} - \frac{C_2^2 Pr^{4n} E^2}{4A^3} \left(\frac{Ra_\lambda}{Re_\lambda^3} \right) + O(\epsilon_1^2). \tag{D5}$$

Variation of (D5) with Re_λ, for $Pr = 1$ and $Ra_\lambda = 1.07 \times 10^5$, is shown in figure 9 to match the variation from the PBBL and the numerical solution of (4.17) at larger values of Re_λ, implying larger shear.

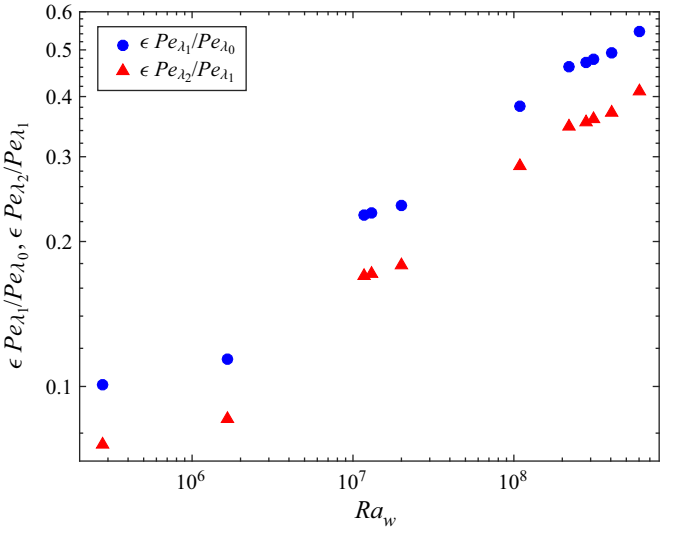

Figure 12. Ratio of terms on the right-hand side of (4.14): blue circles, $\epsilon\, Pe_{\lambda_1}/Pe_{\lambda_0}$; red triangles, $\epsilon\, Pe_{\lambda_2}/Pe_{\lambda_1}$; for the experimental data in the present study.

Appendix E. Upper limit of the analysis

The Pe_{λ_0} term in (4.10) represents the no-shear contribution, while the other terms represent the shear contributions to Pe_λ. Figure 12 shows the variation of the ratios of the successive terms in (4.10) with Ra_w. The contribution of the shear term ϵPe_{λ_1}, compared to the no-shear term Pe_{λ_0}, at the lowest Ra_w, was approximately 10 %. This contribution increases with increase in Ra_w, and becomes close to 55 % at the highest Ra_w. For the ranges of Ra_w and Pr in the present study, both the ratios are much less than 1, and $\epsilon\, Pe_{\lambda_2}/Pe_{\lambda_1} < \epsilon\, Pe_{\lambda_1}/Pe_{\lambda_0}$. The perturbation solution (4.14) is then a power series, and neglecting the second-order term to obtain (4.15) is justified.

We had limited the power-series solution (4.14) to order Re_λ to obtain the scaling (4.15) for Re_{bs}. The present scaling laws are then valid when $\epsilon^2\, Pe_{\lambda_2} \ll \epsilon\, Pe_{\lambda_1}$ in (4.10). In other words, from (4.14) with $C_2 = 0.72$, the scaling laws are valid when

$$Re_\lambda < 2.54\, Ra_\lambda^{2/5}\, E^{3/5}\, Pr^n/A. \tag{E1}$$

Replacing λ_0 in (E1) with (1.5), using (1.3) and (B1), and with $n = 0.5$, we obtain one of the limits of the present analysis as

$$Ra_w < 2.34 \times 10^7\, Pr^{2.6}\, \Gamma^{5.13}, \tag{E2}$$

when $A = 1$.

Similarly, we had also limited the power-series solution (4.25) by eliminating the order ϵ term to obtain the scaling (4.28) for ξ. The present scaling laws are then valid when $I \gg JARa_w^{1/9}$, i.e. when

$$Ra_w^{1/9} < \frac{I}{AJ}. \tag{E3}$$

Replacing I and J, using (4.26) and (4.27), for $A = 1$, we obtain another upper limit of the analysis as

$$Ra_w < 1.12 \times 10^9 \, Pr^{2.6} \, \Gamma^{5.13}. \tag{E4}$$

At any Pr, the limit given by (E4) is higher compared to that given by (E2), and the upper limit of the present analysis at $A = 1$ is then given by (E2). The upper limit of the analysis for $A < 1$ will be higher than that given by (E4), as seen from (E3). For the values $Pr = 5.09$, $\Gamma = 1.71$ and $A = 0.71$ in the present experiments, (E1) implies that the present analysis is valid for $Ra_w < 5.5 \times 10^{11}$; the analysis is then well valid for the present experimental range.

References

Ahlers, G., Grossman, S. & Lohse, D. 2009 Heat transfer and large-scale dynamics in turbulent Rayleigh–Bénard convection. *Rev. Mod. Phys.* **81**, 503.

Blass, A., Zhu, X., Verzicco, R., Lohse, D. & Stevens, R.J.A.M. 2020 Flow organization and heat transfer in turbulent wall sheared thermal convection. *J. Fluid Mech.* **897**, A22.

Castaing, B., Gunaratne, G., Heslot, F., Kadanoff, L., Libchaber, A., Thomae, S., Wu, X., Zaleski, S. & Zanetti, G. 1989 Scaling of hard thermal turbulence in Rayleigh–Bénard convection. *J. Fluid Mech.* **204**, 1–30.

Chilla, F. & Schumacher, J. 2012 New perspectives in turbulent Rayleigh–Bénard convection. *Eur. Phys. J.* E **35**, 58.

Ching, E., Leung, H.S., Zwirner, L. & Shishkina, O. 2019 Velocity and thermal boundary layer equations for turbulent Rayleigh–Bénard convection. *Phys. Rev. Res.* **1** (3), 033037.

Cuba, B., Emran, M. & Schumacher, J. 2010 Aspect ratio dependence of heat transfer and large-scale flow in turbulent convection. *J. Fluid Mech.* **655**, 152–173.

Doering, C.R., Toppaladoddi, S. & Wettlaufer, J. 2019 Absence of evidence for the ultimate regime in two-dimensional Rayleigh–Bénard convection. *Phys. Rev. Lett.* **123** (25), 259401.

Grossmann, S. & Lohse, D. 2000 Scaling in thermal convection: a unifying theory. *J. Fluid Mech* **407**, 27–56.

Gunasegarane, G.S. & Puthenveettil, B.A. 2014 Dynamics of line plumes on horizontal surfaces in turbulent convection. *J. Fluid Mech.* **749**, 37–78.

He, X., Funfschilling, D., Nobach, H., Bodenschatz, E. & Ahlers, G. 2012 Transition to the ultimate state of turbulent Rayleigh–Bénard convection. *Phys. Rev. Lett.* **108**, 024502.

Howard, L.N. 1964 Convection at high Rayleigh number. In *Proceedings of the 11th International Congress of Applied Mechanics* (ed. H. Görtler), pp. 1109–1115. Springer.

Iyer, K.P., Scheel, J.D., Schumacher, J. & Sreenivasan, K.R. 2020 Classical 1/3 scaling of convection holds up to $Ra = 10^{15}$. *Proc. Natl Acad. Sci. USA* **117** (14), 7594–7598.

Lam, S., Shang, X.D., Zhou, S.Q. & Xia, K.Q. 2002 Prandtl number dependence of the viscous boundary layer and the Reynolds numbers in Rayleigh–Bénard convection. *Phys. Rev.* E **65**, 066306.

Niemela, J.J. & Sreenivasan, K.R. 2003 Rayleigh-number evolution of large-scale coherent motion in turbulent convection. *Europhys. Lett.* **62** (6), 829–833.

Ovsyannikov, M., Krasnov, D., Emran, M.S. & Schumacher, J. 2016 Combined effects of prescribed pressure gradient and buoyancy in boundary layer of turbulent Rayleigh–Bénard convection. *Eur. J. Mech. (B/Fluids)* **57**, 64–74.

Pera, L. & Gebhart, B. 1973*a* Natural convection boundary layer flow over horizontal and slightly inclined surfaces. *Intl J. Heat Mass Transfer* **16** (6), 1131–1146.

Pera, L. & Gebhart, B. 1973*b* On the stability of natural convection boundary layer flow over horizontal and slightly inclined surfaces. *Intl J. Heat Mass Transfer* **16**, 1147–1163.

du Puits, R., Resagk, C. & Thess, A. 2013 Thermal boundary layers in turbulent Rayleigh–Bénard convection at aspect ratios between 1 and 9. *New J. Phys.* **15** (1), 013040.

Puthenveettil, B.A., Ananthakrishna, G. & Arakeri, J.H. 2005 Multifractal nature of plume structure in high Rayleigh number convection. *J. Fluid Mech.* **526**, 245–256.

Puthenveettil, B.A. & Arakeri, J.H. 2005 Plume structure in high Rayleigh number convection. *J. Fluid Mech.* **542**, 217–249.

Puthenveettil, B.A., Gunasegarane, G.S., Agrawal, Y.K., Schmeling, D., Bosbach, J. & Arakeri, J.H. 2011 Length of near-wall plumes in turbulent convection. *J. Fluid Mech.* **685**, 335–364.

PUTHENVEETTIL, B.A. & HARSHA, N. 2010 Flux scaling from near-wall coherent structures in turbulent convection. In *Proceedings of the 13th Asian Congress of Fluid Mechanics, Dhaka, Bangladesh*.

QIU, X.L. & XIA, K.Q. 1998*a* Spatial structure of the viscous boundary layer in turbulent convection. *Phys. Rev.* E **58**, 5816–5820.

QIU, X.L. & XIA, K.Q. 1998*b* Viscous boundary layers at the sidewall of a convection cell. *Phys. Rev.* E **58**, 486–491.

RAMA REDDY, G.V. & PUTHENVEETTIL, B.A. 2011 The $Pe \sim 1$ regime of convection across a horizontal permeable membrane. *J. Fluid Mech.* **679**, 476–504.

REEUWIJK, M., JONKER, H. & HANJALIĆ, K. 2008 Wind and boundary layers in Rayleigh–Bénard convection. II. Boundary layer character and scaling. *Phys. Rev.* E **77**, 036312.

ROCHE, P.E. 2020 The ultimate state of convection: a unifying picture of very high Rayleigh numbers experiments. *New J. Phys.* **22** (7), 073056.

ROCHE, P.E., CASTAING, B., CHABAUD, B. & HÉBRAL, B. 2004 Heat transfer in turbulent Rayleigh–Bénard convection below the ultimate regime. *J. Low Temp. Phys.* **134**, 1011–1042.

ROTEM, Z. & CLASSEN, L. 1969 Natural convection above unconfined horizontal surfaces. *J. Fluid Mech.* **39** (Part 1), 173–192.

SCHEEL, J.D. & SCHUMACHER, J. 2017 Predicting transition ranges to fully turbulent viscous boundary layers in low Prandtl number convection flows. *Phys. Rev. Fluids* **2**, 123501.

SHEVKAR, P.P., GUNASEGARANE, G.S., MOHANAN, S.K. & PUTHENVEETTIL, B.A. 2019 Effect of shear on coherent structures in turbulent convection. *Phys. Rev. Fluids* **4**, 043502.

SHEVKAR, P.P. & PUTHENVEETTIL, B.A. 2022 Boundary layer velocity field in turbulent convection. *J. Fluid Mech.* (submitted).

SHI, N., EMRAN, M.S. & SCHUMACHER, J. 2012 Boundary layer structure in turbulent Rayleigh–Bénard convection. *J. Fluid Mech.* **706**, 5–33.

SHISHKINA, O., HORN, S. & WAGNER, S. 2013 Falkner–Skan boundary layer approximation in Rayleigh–Bénard convection. *J. Fluid Mech.* **730**, 442–463.

SHISHKINA, O., STEVENS, R.J.A.M., GROSSMANN, S. & LOHSE, D. 2010 Boundary layer structure in turbulent thermal convection and its consequences for the required numerical resolution. *New J. Phys.* **12** (7), 075022.

SHISHKINA, O. & WAGNER, C. 2008 Analyis of sheet-like thermal plumes in turbulent Rayleigh–Bénard convection. *J. Fluid Mech.* **599**, 383–404.

SHRAIMAN, B.I. & SIGGIA, E.D. 1990 Heat transport in high Rayleigh number convection. *Phys. Rev.* A **42** (6), 3650–3653.

SKRBEK, L. & URBAN, P. 2015 Has the ultimate state of turbulent thermal convection been observed? *J. Fluid Mech.* **785**, 270–282.

STEVENS, R.J.A.M., POEL, E.P., GROSSMANN, S. & LOHSE, D. 2013 The unifying theory of scaling in thermal convection: the updated prefactors. *J. Fluid Mech.* **730**, 295–308.

STEWARTSON, K. 1958 On the free convection from a horizontal plate. *Z. Angew. Math. Phys.* **9** (3), 276–282.

SUN, C., CHEUNG, Y. & XIA, K.Q. 2008 Experimental studies of the viscous boundary layer properties in turbulent Rayleigh–Bénard convection. *J. Fluid Mech.* **605**, 79–113.

TAI, N.C.., CHING, E., ZWIRNER, L. & SHISHKINA, O. 2021 Heat flux in turbulent Rayleigh–Bénard convection: predictions derived from a boundary layer theory. *Phys. Rev. Fluids* **6** (3), 033501.

THEERTHAN, S.A. & ARAKERI, J.H. 1998 A model for near wall dynamics in turbulent Rayleigh–Bénard convection. *J. Fluid Mech.* **373**, 221–254.

THEERTHAN, S.A. & ARAKERI, J.H. 2000 Planform structure and heat transfer in turbulent free convection over horizontal surfaces. *Phys. Fluids* **12**, 884–894.

URBAN, P., HANZELKA, P., KRÁLÍK, T., MACEK, M., MUSILOVÁ, V. & SKRBEK, L. 2019 Elusive transition to the ultimate regime of turbulent Rayleigh–Bénard convection. *Phys. Rev.* E **99** (1), 011101.

URBAN, P., HANZELKA, P., KRALIK, T., MUSILOVA, V., SRNKA, A. & SKRBEK, L. 2012 Effect of boundary layers asymmetry on heat transfer efficiency in turbulent Rayleigh–Bénard convection at very high Rayleigh numbers. *Phys. Rev. Lett.* **109**, 154301.

VIPIN, K. 2013 Boundary layer velocity field in turbulent convection. Master's thesis, IIT Madras, Chennai.

VISHNU, V.T., DE, A.K. & MISHRA, P.K. 2020 Dynamics of large-scale circulation and energy transfer mechanism in turbulent Rayleigh–Bénard convection in a cubic cell. *Phys. Fluids* **32** (9), 095115.

WAGNER, S., SHISHKINA, O. & WAGNER, C. 2012 Boundary layers and wind in cylindrical Rayleigh–Bénard cells. *J. Fluid. Mech.* **697**, 336–366.

WIENEKE, B. 2015 PIV uncertainty quantification from correlation statistics. *Meas. Sci. Technol.* **26** (7), 074002.

ZHU, X., MATHAI, V., STEVENS, R.J.A.M., VERZICCO, R. & LOHSE, D. 2018 Transition to the ultimate regime in two-dimensional Rayleigh–Bénard convection. *Phys. Rev. Lett.* **120**, 144502.

ZHU, X., MATHAI, V., STEVENS, R.J.A.M., VERZICCO, R. & LOHSE, D. 2019 Zhu *et al.* Reply. *Phys. Rev. Lett.* **123** (25), 259402.

ZHU, X. & ZHOU, Q. 2021 Flow structures of turbulent Rayleigh–Bénard convection in annular cells with aspect ratio one and larger. *Acta Mechanica Sin.* **37**, 1291–1298.